Fall 2022

Disequilibrium Melting of the Continental Crust During Emplacement of the Mt. Princeton Batholith, Central Colorado Volcanic Field

Loren A. Bohannon
Missouri State University, Bohannon97@live.missouristate.edu

DISEQUILIBRIUM MELTING OF THE CONTINENTAL CRUST DURING EMPLACEMENT OF THE MT. PRINCETON BATHOLITH, CENTRAL COLORADO VOLCANIC FIELD

A Master's Thesis

Presented to

The Graduate College of

Missouri State University

In Partial Fulfillment

Of the Requirements for the Degree

Master of Science, Geography and Geology

By

Loren Ashley Bohannon

December 2022

DISEQUILIBRIUM MELTING OF THE CONTINENTAL CRUST DURING EMPLACEMENT OF THE MT. PRINCETON BATHOLITH, CENTRAL COLORADO VOLCANIC FIELD

Geography, Geology, and Planning

Missouri State University, December 2022

Master of Science

Loren Ashley Bohannon

ABSTRACT

Assimilation and crystallization are difficult to constrain at magmatic boundaries, including the interactions of magma with the surrounding country rock. The assumption of the relationship between a magma and what it is intruding upon is relegated to homogenous bodies or epizonal plutons. Realistically, wall rock influences chemical heterogeneity and isotopic variance at the outcrop scale and changes depending on distance from the magma-wall rock interface. Here, we present a case study of the 35 Ma Mt. Princeton Batholith and the host Precambrian rocks of the Central Colorado Volcanic Field. We assess chemical heterogeneity by whole rock and mineral trace element and isotope geochemistry, U-Pb zircon geochronology, and mineral assemblages in thin section at varying distances from the interface of the batholith with the wall rock. Two transect locations were selected that provide the best-defined contacts between the wall rock and the Mt. Princeton Batholith containing one sample from the host rock and 7-10 samples from the granite. We present a quantitative model for disequilibrium melting versus crystallization during magma emplacement. We suggest the percentage of zircons with Precambrian age cores included in the granitic body versus magmatic age cores represents the volume of magma affected by the wall rock melting. Granites range in age from 34.1 ± 0.6 Ma to 34.7 ± 0.3 Ma. Precambrian rocks contain two zircon intercept ages, averaging 1600 Ma, and 35 Ma showing evidence of partial resetting, metamorphism, and discordance. Zircon ranges in U-Th ratios from 0.097 - 40.3. Potassium feldspars in the host rock contain Sr contents from 3.9 ppm to 528 ppm and Rb from 4 ppm to 326 ppm. In granites, Sr ranges from 59.4 ppm to 723.9 ppm and Rb from 11.5 ppm to 174.6 ppm. Granite samples nearest to the wall rock contain K-spar inherited from the host where, as distance from the interface increases, these crystals become less prevalent. Modeling trace elements contents and Sr isotopic ratios of potassium feldspar, along with U-Pb zircon geochronology quantifies disequilibrium melting of Precambrian wall rock during emplacement of granitoid composition magmas. These data provide insight into the thermal state of the crust, where a magma partially melted the wall rock, creating a mixing zone at the interface.

KEYWORDS: Mt. Princeton, geochronology, isotope geochemistry, granite, wall rock

DISEQUILIBRIUM MELTING OF THE CONTINENTAL CRUST DURING EMPLACEMENT OF THE MT. PRINCETON BATHOLITH, CENTRAL COLORADO VOLCANIC FIELD

By

Loren Ashley Bohannon

Master of Science, Geography and Geology

A Master's Thesis
Submitted to the Graduate College
Of Missouri State University
In Partial Fulfillment of the Requirements
For the Degree of Master of Science, Geology

December 2022

Approved:

Dr. Gary Michelfelder, Ph.D., Thesis Committee Chair

Dr. Matthew McKay, Ph.D. Committee Member

Damon Bassett, M.S., Committee Member

Julie Masterson, Ph.D., Dean of the Graduate College

ACKNOWLEDGEMENTS

The author would like to extend recognition to faculty and staff of Missouri State University's Department of Geography, Geology, and Planning for their assistance and expertise during the development of this project. Missouri State University's Graduate College is also appreciated for funding provided toward this project. We also thank MSU undergraduate students Connor Pardee and Anna Steiger for assistance in the laboratory and the field. Thanks extends to committee members Dr. Matthew McKay and Damon Bassett for thorough input on this paper. Discussions with Gary Michelfelder, Matt McKay, and Damon Bassett were invaluable in developing this project during the global pandemic. Additional laboratory resources were provided by Barry Shaulis at University of Arkansas, Fayetteville, and Frank Ramos at New Mexico State University. Additional thanks to Jamie Bohannon for her support and excitement over a career that was undervalued by others.

I dedicate this thesis to Mason Sanborn, my quiet strength, and to Miko, the service dog, for her tireless companionship and service in the lab, the field, and every late night.

TABLE OF CONTENTS

LIST OF TABLES

LIST OF FIGURES

INTRODUCTION

Assimilation and crystallization are difficult to constrain at magmatic boundaries, including the interactions of magma with the surrounding country rock (Mills et al., 2009). Even though assimilation and fractional crystallization is a well-documented process, the interactions between granitic magmas and country rock and the consequences of disequilibrium melting on magma composition is poorly understood (Coleman et al., 2004). The assumption of the relationship between a magma and the intruded country rock is relegated to homogenous bodies or epizonal plutons (Coleman et al., 2004). However, melting of the wall rock produces a wide range of magmatic compositions, in turn, producing diverse lithologies within granitic bodies. Wall rock composition influences chemical heterogeneity and isotopic variance at the outcrop scale and changes depending on distance from the magma-wall rock interface. Inheritance occurring at the magma-wall interface is the focus of this project. This study investigates, through the physical and chemical relationships of the interior and exterior of the pluton, the presence of bulk incorporation of the wall rock and partial melting through melt inclusion. The heterogeneity of a pluton should demonstrate a mixing of material produced through assimilation and disequilibrium melting. These data derived from the chemical and physical relationship of the interior and exterior of the pluton offer insight to important processes to understand pluton intrusion and emplacement. Thus, this project explores the trace element, mineral, and isotopic exchange at the magma-wall rock interface through investigation and quantification of wall rock melting during emplacement and storage of a granitic body. Specifically, we determine the ages, compositions, and isotopic ratios of the whole rock granites and mineral phases at distance into the body of the pluton. This is utilized to test the hypothesis that the thermal state of the crust and

melt evolution of mineral phases can be determined during magma intrusion by quantitatively modeling trace element distribution and changes in radiogenic isotopic ratios with distance away from the magma-wall rock interface. To this extent, isotopic exchange was recorded by the percent by volume and isotopic composition of zircon and k-spar with ages and isotopic ratios in equilibrium with the wall rock. A combination of field methods, petrography, mineral trace element analysis, isotopic radiogeochemistry, geochronology, and computer modeling were used to study these granitic magmas. Textural analysis of whole rock granites and mineral phases were used to constrain the paths from the melting region of the bulk rock into the body of the batholith. These data obtained through these methods are presented as a case study of the Mt. Princeton Batholith and surrounding gneissic complexes in central Colorado, where the clear distinction between the inner and outer portions of the magma-wall rock interface was crucial in recording the significance of change with distance away from the boundary. The previous work in the area has covered large areas around Mt. Aetna and includes chemical analysis of the ignimbrites of the area and moderate geologic mapping (Mills and Coleman, 2013; Zimmer and McIntosh, 2012).

BACKGROUND

Geologic (tectonic) Background of Central Colorado Volcanic Field

The termination of Laramide orogeny in the Eocene left uplifts and paleo valleys in the vicinity of the central Colorado volcanic field (CCVF). The CCVF was constructed across basin fill and paleo topography, it was then that the area saw a temporal disconnect between pluton building and ignimbrite eruption (McIntosh et al., 2004; Mills and Coleman, 2013). The 38-29 Ma CCVF is defined as a series of eruptive centers and volcaniclastic products in the Sawatch Range of the Arkansas River Valley, the Front Ranges, the Wet Mountains, the Northern Sangre de Cristo Range, South Park, and the ignimbrite remnants in the Castle Rock area of the High Plains. Between 30 and 26 Ma, the upper Arkansas and San Luis Cristo basins of the Rio Grande Rift began to subside and the Sangre de Cristo and Sawatch ranges uplifted creating a drainage net that allowed pyroclastic flows to travel lengthy distances. As the Arkansas rift basin continued to subside, this drainage was split longitudinally. Presently, the volcanic field is a discontinuous remnant consisting of widely sprawling outcrops of similar age and lithology with common physical, temporal, and geochemical characteristics whose separation was caused by block faulting and erosion (Steven and Epis, 1968). The driving magmatism in this region is currently unknown, or rather undecided. The largest residuum of the CCVF is currently named the Thirty-nine Mile volcanic area located west of the study area in the central CCVF. Silicic volcanism occurred in the Sawatch Uplift 37 to 33 Ma in seven large region ignimbrite sheets and flows (Lipman, 2007). The bulk of these traveled eastward to the Thirty-nine-mile volcanic area but also rested in, and slightly west of, the Sawatch uplift around the Mt. Princeton Batholith (Fig. 1). These seven layers were mapped and analyzed by Epis and students at the

Colorado school of mines and C.E. Chapin and the students at the New Mexico institute of mining and technology. Four of the seven flows are identified at the border of the Sawatch Range but are often obscured by weathering and downfaulting in the volcanic calderas.

The Mt. Princeton Batholith

During a period of eruptive quiescence, noted by the lack of ignimbrites in the Thirty-nine Mile Volcanic Field, the 36 Ma Mt. Princeton batholith intruded and crystallized into the surrounding volcanic units identified as ignimbrite sequences and wall tuffs of the Aetna caldera (Fig. 2) (Mills and Coleman, 2013). This pluton's collection of granitoids is the oldest intrusive unit in the volcanic field post Laramide. This 36-35 Ma Mt. Princeton Batholith is located between Mt. Harvard to the north and Mt. Antero to the south in the central Colorado area. The batholith is part of the Sawatch uplift directly west of the Arkansas River Valley that runs roughly north–south along the main fault of the Rio Grande rift system (Fig. 1) (Lipman, 2007). It is divided into an interior quartz monzonite with multiple phases, identified by Shannon (1988), and two texturally and compositionally diverse border units (Mills and Coleman, 2013; Shannon, 1988). Interior and border units are collectively referred to as Mount Princeton Quartz Monzonite (Mills and Coleman, 2013). The Mount Princeton Quartz Monzonite abuts Precambrian age heterogenic gneisses. Mt. Princeton magmatism includes three large leucogranites that intruded at 30 Ma, the Antero, California, and North Fork that crosscut the older Mount Princeton Quartz Monzonite (Mills and Coleman, 2013). Mills and Coleman (2013) suggested the size of the batholith potentially supplied more heat to the crust, which altered the geothermal gradient and decreased the temperature gradient across the wall rock- magma interface due to a range in TIMS U-Pb zircon ages to analyze samples from the batholith interior.

These ages range from 35.8±0.09 Ma to 35.37±0.1 Ma. The 430 ka range in ages was accepted as the assembly time for this portion of the Mount Princeton Quartz Monzonite as it was observed to have passed through zircon saturation temperatures (~750 ℃) to biotite closure (~300 ℃) within uncertainty (Mills and Coleman, 2013). However, Zimmerer and McIntosh (2012) report dates of the outer interior quartz monzonite as 35.57-33.33 Ma focusing on LA-ICP-MS analyzed U/Pb zircon data. There was a variation of dates for the Mount Princeton Quartz Monzonite reported in previous studies of Zimmerer and McIntosh (2012) reporting a weighted mean of 36.38 ± 0.40 Ma and Mill and Coleman (2013) reporting a weighted mean of 35.80 ± 0.09 Ma; this project intended to further constrain these ages. The other case is Mount Aetna Quartz Monzonite for which Zimmerer and McIntosh (2012) report a weighted mean of 36.40 ± 0.35 Ma and Mills and Coleman (2013) report a weighted mean of 34.95 ± 0.04 Ma; The latter attributes this to variation in the grain selection process and the former covering a greater geographic area.

Mount Princeton Quartz Monzonite. Members associated with the Mount Princeton Quartz Monzonite include a range of granites similar in composition to be grouped as the like. Mount Princeton finer grained quartz monzonite subunit, Mount Princeton Porphyritic k-feldspar subunit, Mount Princeton quartz monzonite interior subunit, and the Mount Princeton Quartz Monzonite are included in this range of granites. Ages range from 36.38 ± 0.40 Ma to 35.80 ± 0.09 Ma (Mills and Coleman, 2013; Zimmerer and McIntosh, 2012). Commonly rocks are grey, medium to coarse grained, equigranular, and homogenous. Hornblende and biotite with phenocrysts locally >4 mm create porphyritic textures. Some rapakivi texture is present in hand sample. Xenoliths and common cognate inclusions with aplite dikes 1 to 6 inches wide that are abundant and widespread. These units have metamorphosed the Paleo Sedimentary rocks within

50 to 300 ft of their contact to form hornfels containing the minerals forsterite, diopside, cordierite, andalusite, and other contact metamorphic minerals (Brock and Barker, 1972).

Border Granites and Gneisses. The Kroenke Granodiorite is a light-grey, medium grained, foliated to massive neatly equigranular biotite granodiorite. Locally includes quartz monzonite and quartz diorite and is trachytoid in part. There were exceptionally clean faces with sparse Fe staining. The Browns Pass Quartz Monzonite is a pink or buff beige, medium to coarse grained, foliated to massive biotite quartz monzonite and granite. At these border units a contact between former and foliated gneiss / gneissic breccia underlaying glacial deposit is noted and textures vary across a 5 square meter area as material diverges in assimilation and appearance including highly weathered, brecciated, vesiculated, schist/phyllite-like, granitic, and gneissic.

Gneisses. The Precambrian formations surrounding the granites consist of the Complex of brecciated Gneisses. They are a heterogeneous mixed of blocks of foliated and massive granitic rocks, augen gneisses, hornblende diorite, coarse grained muscovite schist, and amphibolite that was intruded and cemented by multiple intrusions of medium to coarse grained granitic rocks and pegmatites with large schist lenses. Gneissic Granites are chiefly fine-grained brown, pink, or gray. Foliation is faint but distinct and defined by lines or lenses of biotite and sub-equigranular biotite-bearing rocks. Fragmental blocks of this unit are very abundant in Complex of brecciated Gneisses (Brock and Barker, 1972).

METHODS

Field Sampling Framework and Strategy

Whole rock and bulk zircon samples were focused along two transects within 800 m of the contact between the Mt. Princeton Batholith and the Precambrian host rock to understand the scale of pluton-wall rock interaction. Transect locations were selected to provide the best-defined contacts between the wall rock and the Mt. Princeton Batholith to assess potential pluton contaminants. The first located in the Mt. Harvard quadrangle near Silver Creek, following the trail south from N. Cottonwood Creek into Avalanche Gulch (beginning at UTM 13S 0387362E/4293628N and ending at UTM 13S 0387831E/4293877N). The second is located in the Bueno Vista quadrangle 1.5 km down a pack trail into Bald Mountain. Zircon samples were taken from the interior of the pluton, the Precambrian contact, inclusion-rich zones, and any located pegmatites (beginning at UTM 13S 0387503E/4303419N and ending at UTM 13S 0387547E/4303395N). One transect was chosen for a hyper focused study, determined by which contact could be precisely located and tracked along outcrop exposures at the surface. Sampling from this transect includes one sample from the host wall rock and 17 samples from the Mount Princeton Granite at intervals of 1-3 meters. Five zircon samples were collected from the 17 samples. The second transect is composed of 13 samples including six zircon samples. Hand samples were collected at 1 m intervals for thin section and a zircon sample was taken every 8-10 m for bulk preparation. A total of 30 whole rock samples were collected and 12 viable bulk zircon samples were collected.

Zircon U-Pb Geochronology and Trace Element Analysis

Zircon mineral grains were separated using standard manual mechanical crushing techniques and density separation methods including crushing, sieving, Wifley table separation and magnetic separation at Missouri State University. Following this, the <60 mesh sieved fraction was sent through the Frantz Isodynamic Separator with increasing dynamic angle and amplification to remove magnetic separates and impurities. Non-magnetic separates were further separated by heavy liquids separation using lithium sodium tungstate. Individual grains were picked under microscope to ensure purity and placed on tape mounts. Granite samples contain 75-100 zircons per sample and the Precambrian host wall rock included 25-30 zircons. U-Pb isotope ratios within zircon were obtained at the University of Arkansas using an ESI NWR 193 nm Excimer Laser Ablation System coupled with a Thermo Scientific iCapQ Quadrupole Mass Spectrometer. Laser ablation was accomplished with a 25 μm diameter spot size with laser fluence of 2.0-2.2 J/Cm^2 at 10 Hz for 15 seconds of integration. On peak dwell times were adjusted to give the best precision on the U/Pb and Pb/Pb ratios for an average zircon composition. The value, uncertainty, and scatter of zircon standards during the analytical session was 1%–2% (2 standard deviations [2σ]). The primary zircon reference material analyzed was 91500 (1062.4±0.8 Ma). Plesovice (337.1±.0.1 Ma) and Mud Tank (732 Ma; Woodhead and Hergt, 2007) were used as secondary zircon reference materials. A selection of analyses with acceptable precision, discordance, and in-run fractionation are presented in Table 1 with the full dataset presented in the online supplement. Analyses significantly above ^{204}Pb (common lead) detection limits (~600 cps) were rejected. Systematic uncertainty was propagated using quadratic addition incorporating the internal and external reproducibility of the reference materials and data was reduced using the Iolite4 software (Patron et al., 2011). The reported U-Pb age for each

sample is a weighted mean of 34-1600 Ma individual zircon U-Pb analyses. Due to all samples possessing Mesozoic or younger crystallization ages, $^{206}Pb/^{238}U$ ratios were used to calculate weighted mean ages. Weighted mean ages were calculated using the IsoPlot 4.0 software (Ludwig, 2003).

Trace element content of zircon was determined for all zircon grains at the University of Arkansas using the same conditions as for the U-Pb isotope analyses. The NIST610 and NIST612 glasses were used as external calibration standards. The 91500-zircon reference mineral was used as a secondary calibration standard. Quantitative results for 25 elements were obtained through calibration of relative element sensitivities of the calibration standards. Off-line selection and integration of background and analyte signals, and time-drift correction and quantitative calibration were performed using the Iolite4 reduction software (Paton et al., 2011).

Whole Rock Major and Trace Element Analysis

Twenty-seven standard thin sections and nine polished sections of whole rock samples were used to evaluate basic mineral textures, composition, and petrology of the study area, and classify the rocks, the conditions under which they formed, to determine phases for further analysis. Based on thin section analysis, 15 samples were analyzed for major and trace element contents. Whole rock major element contents were determined at the University of Iowa using a Rigaku Primus IV Sequential Wavelength Dispersive X-Ray Fluorescence Spectrometer. Precision for major element analyses was better than 1%. Trace element contents including the rare earth elements (REE) were determined at Missouri State University using an Agilent 7900 quadrupole ICP-MS. Samples were ground to a powder using a steel jaw crusher and tungsten carbide planetary ball mill. Digestion details and analytical procedures are like those described in

Liu et al. (2008). An aliquot of 50 mg of sample was dissolved in a sequence of acid digestions. Initial digestion was in 1.5:1.5 mg solution of HF and HNO_3 at 210°C for 24 hours in a closed Teflon beaker on a hot plate. When the solids were completely dissolved, the acid was evaporated, and the process was repeated for two additional rounds of digestion. The second digestion contained 3 ml of HNO_3 and the third with 3 ml of HCl. A final round of digestion contained 3 ml of HNO_3 in an enclosed beaker for 12 hours. One milliliter of H_3BO_3 was added to the sample then diluted to 100 grams. An aliquot of the digested solution of 15 ml was analyzed by ICP-MS and corrected for spectral interferences. Three USGS reference materials were used to calibrate the analysis and correct for analytical drift: STM-2, BCR-2, and RGB-2. Further quality control was assured by co-analyzing the reference materials with the unknowns. All reference material analyses overlap with certified values at 2σ.

The concentration of Ti-in-zircon and Al-in-hornblende is temperature dependent and can be defined as a thermometer based on the experimental work of Watson et al. (2006), Watson and Harrison (2005), Ferry and Watson (2007) and Ridolfi et al. (2010; 2012) and natural samples. The Ti-in-zircon thermometer determines the temperature of zircon crystallization based on the activity of TiO_2 and SiO_2 using the following equation:

$$T(K) = \frac{-4800 \pm 86}{\log Ti(ppm) + log\alpha_{SiO2} - \log\alpha_{TiO2} - (5.711 \pm 0.072)}$$

Proper application of the thermometer mentioned in requires knowledge of α_{TiO2} and α_{SiO2} at the time of zircon crystallization and zircons are often inherited and not in equilibrium with the magma (Claiborne et al., 2010). Additionally, zircon record the composition in equilibrium at the time of crystallization and not necessarily the evolution of the magma, which changes α_{TiO2} and $\alpha_{SiO2.}$ Here we assume zircon crystallization occurs contemporaneously with hornblende and the effects of crystallization and magma evolution are ignored. We assume this because zircon and

hornblende are both include in alkali feldspar, but we cannot be certain how these compositions varied. Considering the ubiquity of quartz as a subhedral phase in the batholith, we hold α_{SiO2} at 1.0, thus maximizing the temperature estimates. The presence of titanite as euhedral crystals suggests α_{TiO2} was high (Hayden and Watson, 2007; Sommer et al., 2022). Regardless Ti-in-zircon temperatures are modeled with a range of α_{TiO2} from 0.1 to 1.0. Based on these calculations, α_{TiO2} is assumed to be between 0.8 and 1.0 providing temperatures between 609-852°C (Fig. 6).

Mineral Major and Trace Element Analysis

Major element contents of alkali feldspar, plagioclase, hornblende, and biotite were determined by electron probe microanalyzer (EPMA) at the University of Iowa using JOEL JXA-8230 Superprobe microanalyzer (EMPA) using five wave-length-dispersive spectrometers and eight large-format diffracting crystals. All analyses were performed using an accelerating voltage of 15 keV with a current of 20 nA with a one-micron spot size. The run-time was 2.5 minutes for feldspar and 4.5 minutes for hornblende and biotite with an on-peak dwell times of 15-30 seconds and a background dwell time of 5 seconds. Fifteen to twenty crystals per phase were analyzed from three granitoid samples and one wall rock sample. Core-to-rim transects were determined for five feldspars per samples. All other crystals contain a minimum of 3 spots representing the core, rim, and an intermediate point. Major element contents for hornblende and biotite were calibrated using Kakanui Hornblende (NMNH# 143965; Jarosewich, 2002) and the Astimex Cr-Pyrope reference material. Biotite was calibrated using Astimex chlorite. Feldspar major element contents were calibrated using the Astimex Labradorite Plagioclase reference material and microcline (NMNH#143966; Jarosewich, 2002).

Potassium feldspar grains mounted in epoxy pucks and polished to expose the surface were analyzed via LA-ICPMS at the University of Arkansas to conduct trace element analysis for 27 elements (14 REE's & Ba, Th, Nb, Y, Hf, Ta, U, Pb, Rb, Cs, Sr, Sc, Zr). Spot analysis of 25 µm on each grain was performed. Concentrations were calculated relative to the NIST610 and NIST612, and Z-91500 standards and reduced using the Iolite 4 - Igor software program (Paton et al., 2011).

Whole Rock and Mineral Radiogenic Isotope Analysis

Whole rock isotopic analysis was conducted on six whole rock samples including five granitoid samples and one Precambrian wall rocks sample. Whole rock Sr isotopic analyses were acquired by Thermal Ionization Mass Spectrometry (TIMS) on a VG Sector 54 and analyzed by five Faraday collectors in dynamic mode at the Johnson Mass Spectrometry Laboratory New Mexico State University, Las Cruces. Calibration of $^{87}Sr/^{86}Sr$ ratios was calculated using the $^{86}Sr/^{88}Sr$ ratio analyzed at 3.0 V aiming intensity and normalized to 0.1194 using NBS 987 Standard (0.710298 ± 0.000010) to monitor the precision of the analyses. Sr was isolated using Sr-Spec resin column chromatography by the method described in Ramos and Reid (2005). Neodymium and lead were analyzed on a ThermoFinnigan Neptune multi-collector ICP-MS equipped with nine Faraday collectors and an ion counter. Neodymium was separated using REE resin column chromatography using the digested split of prepared sample for Sr chromatography. Nd isotopes were normalized to $^{146}Nd/^{144}Nd = 0.7219$ and results for JNDi-1 were $^{146}Nd/^{144}Nd = 0.512137 \pm 0.000009$ for five analyses. Pb isotopes were separated from the same digested samples used for Sr and Nd isotope ratios. Lead separations used ~2 mL of anion exchange resin in a high-aspect ratio glass column with an eluent of 1N HBr and 7N HNO_3. Purified samples

were then dried and re-dissolved in 1 mL of 2% HNO_3 containing 0.01 ppm Tl. The standard NBS 981 ($^{208}Pb/^{204}Pb \approx 36.662 \pm 0.002$, $^{207}Pb/^{204}Pb \approx 15.462 \pm 0.001$, $^{206}Pb/^{204}Pb \approx 16.928 \pm 0.001$) was used for accuracy corrections and to monitor precision of the analyses. The values measured for NBS 981 were within the error of published ratios for NBS 981 (Todt et al., 1996), and therefore, corrections were not applied to unknown sample.

Individual feldspars were also handpicked from sieve fractions crushed and separated for zircon U-Pb geochronology. Feldspars were etched in 10% HF acid for 20–30-minute intervals. Crystals were then rinsed in distilled water and sonicated to obtain crystals free of adhering materials. The mineral analysis consisted of 20 crystals of orthoclase (COT 2, 6, 7, 8, 14, 21, 27, and 33) ranging from 0.7 - 26.0 mg. Individual clean crystals were dissolved using hydrofluoric, nitric, and hydrochloric acids. Crystals with masses greater than 5 mg were separated using standard column chromatography. Crystals with masses less than 5 mg were separated using micro-columns. Strontium was purified using cation exchange chromatography and 2.5N hydrochloric acid. Lead was purified using 1N hydrobromic acid and anion exchange chromatography. Lead was analyzed using multi-collector inductively coupled plasma mass spectrometry with Pb isotopes normalized to NBS997 $^{205}Tl/^{203}Tl=0.41892$ and Sr was analyzed using thermal ionization mass spectrometry with Sr normalized to $^{86}Sr/^{88}Sr=0.1194$ at the Johnson Mass Spectrometry Laboratory at New Mexico State University.

RESULTS

Petrography

Standard thin sections for the following samples were analyzed by polarized microscopy at 10x and 40x magnification: COT 1-4, 6-11 for transect 1 and COT 14-15, 17-18, 20-22, 24, 26-27, 29-30, 32-33 for transect 2. Additional Photomicrographs and Backscatter Electron Images (BSE) of the samples by transects are presented in Appendix 1 and 2.

Transect 1 Precambrian Wall Rock. Samples COT 1-4 demonstrate idioblastic gneissic textures within the Precambrian gneisses of the wall rock with proximity to magma-wall rock interface increasing as sample number increases. Essential minerals are ~1-4mm subhedral plagioclase are present with polysynthetic and albitic twins and form close to ~0.2-3mm anhedral quartz with notable undulatory extinction, this is then followed by less abundant orthoclase, which are few in number and ~0.5mm with crosshatch twinning indicative of microcline. 04-4mm subhedral Ti-rich biotite has a high second order birefringence of which was almost mistaken for abundant clinozoisite. Plagioclase altering in the center of several grains to sericite. Seritization is pervasive throughout the samples along grain boundaries of plagioclase and quartz as well. Clusters of small quartz grains form alongside this alteration. There is a distinctive foliation of minerals that biotite and secondary chlorite follows closely. Apatite and titanite are present in an accessory fashion. Sample COT 2 differs in the introduction of myrmetic and perthitic textures as exhibited in Appendix 1. By sample COT 3, as approaching the contact with the interior, texture becomes wholly altered and clearly foliated in both hand sample and thin section. However, size of grains decreases to no larger than 1mm in length. Zoisite is present here in very dark blue and surrounded by lighter micas (chlorite, muscovite, and saussurite).

COT 4 has more noticeable concentric zoning in plagioclase grains, with some anhedral grains within the euhedral plagioclase. Pervasive seritization and zoisite is present within some grains. Quartz is anhedral to subhedral with seriate hiatal crystal sizes up to ~5mm grains. Microcline of ~0.5-2.2mm formed along the boundaries of plagioclase and is far less abundant than plagioclase and quartz. Subhedral to euhedral biotite is present as varietal variations altering to Ti-rich ilmenite and chlorite near hornblende. Accessory minerals include titanite as well as apatite and zircon which are mostly present in the plagioclase feldspar.

Transect 1 Interior Monzogranite – Quartz Monzonite. Samples COT 6-11 demonstrate textures for the interior monzogranite (nominally the Mount Princeton Quartz Monzonite) with distance into the interior increasing as sample number increases. Overall, the megascopic samples are holocrystalline, hypidiomorphic granular, and characteristically leucocratic throughout. Modal composition suggests a petrographic name as biotite-bearing monzogranites, supported by the habitually felsic, silica-rich, appearance with the presence of titanite, ilmenite, Ti-oxides, apatite, and zircon as accessory minerals. Over the boundary, COT 6, quartz increases in size and abundance as plagioclase feldspar improves in shape to mostly euhedral. COT 7 has ~2mm grains of biotite, ~0.3-0.5mm titanites with zircon inclusions, amphibole, and apatite. This sample is close in proximity to a fault and thus heavily altered with cumulate fracture fill of mostly quartz (Appendix 1). COT 8 has notable plagioclase to sericite alteration. Titanite increases in size up to 1.6mm. Amphibole also increases in size and abundance to sub-euhedral grains of ~2.5mm with alteration along the grain boundaries to epidote and chlorite. Hand samples contain xenoliths and quenched magmatic inclusions as well as rapakivi textures as plagioclase rims potassium feldspar within inclusions. Farther towards the

interior, the abundance of quartz increases, and the abundance of secondary alteration products decrease.

Transect 2 Precambrian Wall Rock. Samples COT 14-15 demonstrate textures within the Precambrian gneisses of the wall rock and the contact, with proximity to magma-wall rock interface increasing as sample number increases. In COT 14, subhedral plagioclase grains measure at ~0.4-2.5mm and demonstrate polysynthetic and simple twinning. Quartz is at greater abundance but only ranges up to 2mm. Potassium feldspar displays grid iron twinning indicating the presence of microcline in a few large grains ~15%. Biotite forms in clusters around the feldspars at ~0.2-0.6mm and show Ti-rich alteration as well as chloritization. Amphibole is present as hornblende altering to epidote on select areas around the grain boundaries. Some apatite grains are clean and some include zircon with a sizable glomerocryst of amphibolite. COT 15 is located on the contact between the interior and exterior of the pluton. There is a severe increase in alteration products including zoisite, chlorite, and sericite. K-feldspar outnumbers quartz which is, in turn, more abundant than plagioclase feldspar.

Transect 2 Interior Monzogranite – Quartz Monzonite. Samples COT 17-33 demonstrate textures for the interior monzogranite (nominally the Mount Princeton Quartz Monzonite) with distance into the interior increasing as sample number increases. At COT 17 the grain size and shape increase but the abundance of potassium feldspar significantly decreases. By COT 18 the section is primarily composed of quartz and plagioclase. Zoisite is present along grain boundaries of plagioclase and biotite and withing plagioclase grains. Biotite is altering to chlorite. Amphibolite glomerocrysts with oxides are present in this sample as well. COT 20 displays a slight increase in the size and abundance of potassium feldspar as quartz decreases. Sericite, chlorite, and clinozoisite are present as alteration products. COT 21, to the end of the

transect, oxides are clustered tightly around amphibolite and biotite increases in size, becomes more euhedral, and has less visible alteration. Essential minerals are relatively equal in abundance. COT 30 demonstrates a Precambrian lens within the interior. Amphibolite and oxides increase in size, with hornblende more abundant. Plagioclase and quartz increase in abundance as microcline becomes less frequent but remains sub-euhedral. Biotite averages ~2.2-3mm and shows chloritization. Zircon and apatite are included in the biotite grains, likely from inheritance. COT 30 has little variation from COT 21 other than a drastic decrease in secondary alteration products. COT 33 displays zoned zircon grains and zircon trapped as melt inclusions within the apatite. 3-6mm subhedral essential minerals. Large, hardly altered, biotite forms around the boundaries of plagioclase.

Zircon U-Pb Geochronology

A total of 496 zircon grains were analyzed via spot analysis from 12 bulk samples including five samples from the Precambrian host rock and seven from the batholith interior. Results from zircon U-Pb geochronology are presented in Table 1 and illustrated in Figure 3. The zircons analyzed in this study are broadly consistent with previous studies (Mills and Coleman, 2013; Zimmerer and McIntosh, 2012). Data from previous studies for U-Pb zircon ages are provided in Appendix 4. Weighted mean ages presented in Table 1 are interpreted as crystallization/emplacement ages and exclude blended ages determined in the Precambrian samples, and old ages obtained from premagmatic zircon cores and occasional young ages interpreted to be related to loss of radiogenic Pb (Appendix 4).

Igneous Pluton Interior. The Mt. Princeton monzogranite contains subhedral to euhedral elongate zircons with no visible inclusions. Interior granitic samples range in age from

34.20±0.08 Ma to 35.72±0.09 Ma (Fig. 3). There is no correlation with distance from magma-host rock interface. The weighted mean ages reflect the complex history of zircons. Almost every sample included 5 or fewer spot analyses that showed Pb loss or other related exceptional outliers. When excluded, the ages remained appropriate and lowered the MSWD.

Metamorphic Pluton Exterior. Precambrian host rock samples contain zircons with magmatic cores and metamorphic rims. Two ages are suggested based on Concordia diagrams, cores are aged 1600±20 Ma reflecting zircon crystallization whereas rim ages from these zircons range in age from 34-36 Ma and reflect metamorphism during magma intrusion (Appendix 3). Of 447 total spot analyses, 197 represented metamorphic ages indicating a core reading. For all spot analyses on gneissic samples, every point resulted in an appropriate metamorphic core age. It is important to note that concordia diagrams we used to determine which selections were appropriate to exclude whereas the reported ages for all samples is from the weighted mean.

Zircon Trace Element Analysis and Ti-in-Zircon Temperatures

In total, 120 zircons were analyzed for trace element contents consisting of 10 zircon grains of each bulk sample including both interior granitoids and country rock. Elongated grains were selected for analysis to ensure spot did not overlap the spot analyses for zircon geochronology. Results from the trace element analysis are presented in Table 2 and illustrated across Figures 4 to 6. The complete dataset is available in Appendix 5. Zircons from the Mt. Princeton monzogranite contain 12650 to 28375 ppm Hf and Th/U ratios ranging from 0.32 to 1.77. Zircon U contents range from 126-5970 ppm and Th contents range from 193-4284 ppm. There is a general decrease in Th/U ratio with increasing Hf content. Ratios of Yb/Gd, U/Yb, Ce/Yb, range from 8-63, 0.29-7.0, and 0.01-0.1, respectively (Fig. 4). Pronounced negative Eu

anomalies and positive Ce/Ce* anomalies range from 0.15-0.55 and 0.2-402.3, respectively. There is an overall increase in Yb/Gd and U/Yb ratio with increasing Hf content, no correlation with Ce/Yb and Eu anomaly and a negative correlation of Ce/Ce* with increasing Hf contents (Fig. 4).

Precambrian wall rock zircons generally have a higher Hf content (Hf= 1197-27,506 ppm) compared to monzogranite zircons. Metamorphic zircons contain U and Th contents ranging from 312-2412 ppm, and 88-1460 ppm, respectively and are generally higher than the contents observed in the granitoids. Th/U ratios are more variable ranging from 0.06-2.74 and show a decrease overall with increasing Hf content (Fig. 4). Wall rock zircon Yb/Gd (6.15-61.50) and Ce/Yb (0-0.01) ratios are similar to the granitoids (Fig. 4). U/Yb (0.41-6.67) ratios show more variation, but overlap the range observed in the granitoid zircons (Fig. 4). Eu anomalies are generally similar to the granitoid zircons but contain a population that has a more pronounced negative anomaly ranging from 0.06-0.4.

Zircon rare earth element (REE) contents for both the Mt. Princeton monzogranite and Precambrian wall rock zircons are similar and reflect typical zircon REE trends (Fig. 5). Two populations of zircons are present in all samples except COT2 and COT3. The first population represents the typical light REE depleted to heavy REE enriched patterns (Fig. 5). The second population is less prevalent in in the granitoid samples but is common in the metamorphic rock samples with a lower Yb/La ratio and more enriched light REE contents (Fig. 5). The two metamorphic zircon samples, COT2 and COT3 from transect one only contain the depleted light REE content population. Both transects contain less of the population two zircons with distance from the interface (Table 2).

Zircon crystallization temperatures were calculated using Ti-in-zircon (T_{TiZ}) using the equation of Ferry and Watson (2007). A range in αTiO_2 and αTiO_2 were considered and based on the mineral assemblage of both the Precambrian wall rock and the granitoids, we used αSiO_2 as a constant of 1 and 0.75, and carried out the calculations for αTiO_2 ranging from 0.1 to 1 to get a range of temperatures that closely resemble the average Al-in-hornblende temperature of 755±22˚C. The best fit of temperatures use a αSiO_2 of 1 and a αTiO_2 of 0.9 (Fig. 6). Crystallization temperatures range from 609-1261°C. Granitoid zircons range from 609-1202 °C and Precambrian wall rock zircon range from 666-1261 °C. Zircon crystallization temperatures above 1000°C are not considered due the high Ti contents likely from the presence of inclusions in the zircon. All calculated Ti-in-zircon temperatures, excluding those not considered, are reasonable for felsic magmas and zircon growth in a shallow crustal environment. These temperatures show a weak correlation of increasing temperature with increasing Hf content.

Mineral Trace Element Analysis

A total of 96 spots were analyzed on 24 potassium feldspar grains. Three to four clean and inclusion free grains from eight samples were analyzed. Feldspars range from 3-5 mm in length. Spots were selected in a transect across the mineral grain ensuring contact to any possible core and an average reflecting the entire crystal. Data are presented in Table 3 and illustrated in Figures 7 to 8. A comprehensive data table is included in Appendix 6. K-feldspar from the interior granitoid contain an average range of 1360.8 – 3913.5 ppm of Ba and ratios of Th/U from 0.17 to 3.93. Ratios of Ba/Ce, Ba/La, Sr/Ba, range from 520.93-8689.7, 504.64-5614.7, and 0.1-0.26, respectively (Fig. 7). Transect 1 interior sample ratios range 5275.7-8631.4, 4588-5614.7, and 0.08-0.13 for Ba/Ce, Ba/La, Sr/Ba, respectively. Transect 2 interior sample ratios

range 520.93-8689.7, 504.64-4896, and 0.1-0.26 for Ba/Ce, Ba/La, Sr/Ba, respectively. Within the granitoids, two populations of Eu anomalies exist, a low and high value population. Eu anomaly of K-feldspar range from 0.71-133.04. The higher population consists of COT – 27 (Eu/Eu* = 35.45), COT – 21 (Eu/Eu* = 25.40), COT – 6 (Eu/Eu* = 15.52), and COT – 8 (Eu/Eu* = 24.39), whilst the samples COT – 2 (Eu/Eu* = 7.58), COT – 33 (Eu/Eu* = 8.24), and COT – 15 (Eu/Eu* = 5.05) populate in the lower range. In relationship between Sr/Ba vs Ce/Ba, La/Ba, and Rb/Sr two populations also exist. The higher, belonging to COT 15, the sample located on the contact between granitic body and wall-rock. The other population consists of COT 2, 6, 8, 14, 21, and 27 with COT – 33 lower in value but with a much higher Sr/Ba concentration (Fig. 17).

Precambrian K-feldspar from Precambrian wall rocks display a positive trend of Ba to Sr and a present but less drastic trend of Ba to Ce and La. These contain 2094.6 ppm of Ba and ratio 0.0843 of Th/U. Ratios of Ba/Ce, Ba/La, Sr/Ba, are 4414.7, 5359.3, and 0.0953, respectively (Fig. 8). The border unit of COT 15 located on the interface contains 183.51 ppm of Ba and ratio 2.857 of Th/U. The ratio of Ba/Ce, Ba/La, and Sr/Ba are 94.871, 191.69, and 0.2708, respectively.

Hornblende Major Elements Composition

A total of 72 grains over three samples were analyzed via electron probe microanalyzer (EMPA) for Al-in-hornblende geothermobarometry. Complete results are presented in Appendix 7. Analysis of Mg species hornblende resulted in oxygen fugacity ($\log fO_2$) ranging from -14 to -12 and temperatures values ranging from 678 – 870°C. Continental depth pressures (CDP) range 25 – 168MPa. Overall range of H_2O content of 3.4 – 4.9 wt% can be seen in COT 33 with the

samples at lesser distance from the interface including middling values. (COT 27= 3.7-5: COT 30= 3.7-4.8; COT 33= 3.4-4.9). The fluorine wt% range includes values 0.15 - 0.50 (COT 27= 0.18 – 0.50; COT 30= 0.15 – 0.46; COT 33= 0.16 – 0.44). Chlorine wt% range includes values 0.00 – 0.16 (COT 27= 0.02 – 0.16; COT 30= 0.00 – 0.14; COT 33= 0.01 – 0.13). Al# average of 0.4 is also notable with an overall range of 0.00 - 0.16 (COT 27_{avg}: 0.03; COT 30_{avg}: 0.04; COT 33_{avg}: 0.06).

Mineral Isotope Analysis

A total of 23 inclusion-free, 3-5 mm K-feldspar grains were analyzed from 13 samples for mineral Sr and Pb isotope analysis via TIMS. Results are presented in Table 4 and illustrated in Figure 9. K-feldspar in the interior granitoid average $^{87}Sr/^{86}Sr$=0.709471 and $^{84}Sr/^{86}Sr$=0.056435. Sr isotope ratios range from $^{87}Sr/^{86}Sr$=0.708077 to 0.712148 and $^{84}Sr/^{86}Sr$=0.56364 to 0.56472. Transect 1 interior with a higher average of $^{87}Sr/^{86}Sr$ at 0.70991 and $^{84}Sr/^{86}Sr$ at 0.05645. Transect 2 interior with a lower average of $^{87}Sr/^{86}Sr$ at 0.709031 and $^{84}Sr/^{86}Sr$ at 0.056419. Interior batholith samples average $^{206}Pb/^{204}Pb$= 17.678, $^{207}Pb/^{204}Pb$= 15.492, and $^{208}Pb/^{204}Pb$= 38.231. Pb isotope ratios range from $^{206}Pb/^{204}Pb$= 17.791 to 17.904, $^{207}Pb/^{204}Pb$= 15.506 to 15.516, and $^{208}Pb/^{204}Pb$= 38.079 to 38.161.

Precambrian wall rock averages $^{87}Sr/^{86}Sr$=0.717163 and $^{84}Sr/^{86}Sr$=0.056438 for mineral isotope analysis with a range $^{87}Sr/^{86}Sr$ from 0.708793 to 0.725520. Transect 1 wall rock with an average of $^{87}Sr/^{86}Sr$ at 0.708790 and $^{84}Sr/^{86}Sr$ at 0.056454. Transect 2 wall rock with an average of $^{87}Sr/^{86}Sr$ at 0.721349 and $^{84}Sr/^{86}Sr$ at 0.05643. Precambrian samples average $^{206}Pb/^{204}Pb$= 17.394, $^{207}Pb/^{204}Pb$= 15.452, and $^{208}Pb/^{204}Pb$= 38.478. Pb isotope ratios range from $^{206}Pb/^{204}Pb$= 17.342 to 17.840, $^{207}Pb/^{204}Pb$= 15.448 to 15.516, and $^{208}Pb/^{204}Pb$= 38.111 to 38.656.

Whole Rock Trace Element and Isotope Analysis

Thirteen samples were analyzed for whole rock trace element isotopes via ICPMS. Data are presented in Table 5. A comprehensive data table is included in Appendix 8. The interior granitoid Sr ranges 374.291-538.008ppm. Rb, Ba, La, Pb, Th, and U range 110.307-117.525, 741.996-165.123, 41.443-60.458,15.318-17.196, 19.367-21.474, and 2.606-4.502 respectively. Transect 1 ranges are shorter more concise than the second transect: 374.291-527.446 Sr, 114.021-114.697 Rb, 770.555-865.123 Ba, 41.443-59.72 La, 16.075-17.196 Pb, 20.429-25.002 Th, and 2.606-4.502 U. Transect 2 ranges have a greater range but no inflated error: 482.629-538.008 Sr, 110.307-117.525 Rb, 723.479-865.12 Ba, 50.863-60.458 La, 15.318-16.921 Pb, 19.367-23.235 Th, and 4.076-4.397 U. La/Yb and Sr/Y range 26.62278876- 32.98496659 and 17.35721573- 29.12939747, respectively.

Precambrian wall rock ranges in 106.277-503.68 Sr, 76.535-151.386 Rb, 522.991--1193.29Ba, 28.539-78.035 La, 8.216-36.225 Pb, 6.287-51.598 Th, and 0.351-8.712 U. Transect 1 ranges 403.42-503.68Sr, 76.535-151.386 Rb, 769.199-1193.29 Ba, 49.884-71.528 La, 8.216-17.689 Pb, 6.518-26.723 Th, and 0.733-4.927 U. Transect 2 ranges 106.277-387.74Sr, 86.648-141.517 Rb, 522.991-1044.554 Ba, 28.539-78.035 La, 12.703-36.225 Pb, 6.287-51.598 Th, and 0.351-8.712 U. La/Yb and Sr/Y range 14.9568229-122.4849785 and 1.853744048-89.67151163, respectively.

Whole rock Sr isotope ratios, presented in Table 6, are variable and dependent on if the sample represents the batholith or the Precambrian wall rock. Batholith Sr isotope ratios are restricted with measured $^{87}Sr/^{86}Sr$ ratios ranging from 0.708077 to 0.708297. Pb isotope ratios are more variable ranging from $^{206}Pb/^{204}Pb$= 17.901 to 18.011, $^{207}Pb/^{204}Pb$= 15.521 to 16.05, and $^{208}Pb/^{204}Pb$= 38.266 to 43.055. Sr isotope ratios of the wall rock range from measured $^{87}Sr/^{86}Sr$

ratio of 0.717808 to 0.718533 and has Pb isotope ratios of $^{206}Pb/^{204}Pb$= 17.766 to 18.650, $^{207}Pb/^{204}Pb$= 15.470 to 15.571, and $^{208}Pb/^{204}Pb$= 38.582 to 38.793.

DISCUSSION

Zircon and potassium feldspar compositions and ages from the Mt. Princeton Batholith and the surrounding Precambrian host rocks reflect the magmatic processes during the emplacement of the batholith at shallow crustal levels (Kay et. al., 2010). Hafnium contents of zircons have been shown to be a proxy for the extent of crystallization in silicic magmas. Additionally, zircon Eu/Eu* can be used to track feldspar fractionation. Therefore, systematic variation in both Hf and Eu/Eu* composition combined with Th/U, U/Yb and Yb/Gd ratios reflect both zircon and plagioclase crystallization within the cooling magma and can indicate zircon remobilization during wall rock assimilation (low Hf, low U/Yb, high Eu/Eu*) (Klemetti and Clyne, 2014).

In this chapter, the interpretation of these data is separated intentionally by transect and used to compare the variations within and differences among populations of zircon, K-feldspar, and hornblende. These variations help to determine whether mineral chemistry can be used to ascertain certainty in changes away from magma-wall rock interface. The initial observations suggest a decrease in compositional heterogeneity with distance from the magma-wall rock interface. This is further supported by U-Pb geochronology and Ti-in-zircon temperatures.

The subject of this project being tested is the relict of a batholith - what remains after the physical evidence of the caldera (intracaldera tuff, postcaldera lavas, etc.) has been eroded (Zimmerer and McIntosh, 2013). Whole rock La/Yb and Sr/Y ratios for the batholith interior shows enrichment in LREE and LIL, which is expected of a metaluminous I-type granite sourced from partial melting of mantle deprived mafic underplate and crustal contribution (Michelfelder et al., 2013). $^{87}Sr/^{86}Sr$ ratios <0.708 further support this idea and suggest magmatism is related to

calc alkaline suites. This alone suggests a lower crustal source and is further supported by a relationship between Sr whole rock trace element analysis and $^{87}Sr/^{86}Sr$ isotopic analysis suggest assimilation of about <3% of the wall rock. This indicator of the melt crystallizing faster than it assimilates the host material supports the idea that the magma intruded into a cold country rock creating a quenched margin between the magma and the wall rock. The variation of $^{87}Sr/^{86}Sr$ from the metamorphic wall rock to the interior is likely the result of variation in the parental source was lower in the crust - likely a stable garnet source's signature (Kay et. al., 2010). Additionally, pressures from hornblende indicate a depth of 6 km supporting a caldera forming silicic magma as a feeder to the caldera prior to eruption that originated in the lower crust and emplaced shallowly.

Magmatic Temperatures

Based on the whole rock geochemistry of Mills and Coleman (2013) zircon saturation temperatures were calculated for each of the samples presented in this study. These temperatures suggest that Ti-in-zircon temperatures above 800°C record inherited zircons and suggest zircon crystallization temperatures between 609-775°C reflect crystallization of zircon in equilibrium with the Mt. Princeton Batholith magmas. Together, Ti-in-zircon and Al-in-hornblende temperatures, suggest that zircon growth in the Mt. Princeton Batholith occurred between 750-780°C (Fig. 6). Al-in-hornblende temperatures yield a more limited range than Ti-in-zircon temperatures, but this is to be expected, since zircon growth continues to the solidus and individual zircon ages suggest some inheritance from the Precambrian wall rock. Additionally, zircon growth can initially begin in zircon undersaturated magmas with inherited nucleated zircon which can lead to higher Ti-in-zircon temperatures than what is recorded in thermally

equilibrated hornblende (Harrison et al., 2007; McDowell et al., 2014). Zircon from the Precambrian wall rock samples and samples close to the magma-wall rock interface contain an average higher Ti content than zircons that are crystallized in the magma, and therefore, contain higher estimated Ti-in-zircon temperatures, which in some cases exceed 950°C, which is the calculated zircon saturation temperature (ZST) for the Mt. Princeton Batholith. Zircon temperatures that are lower than ZST represent zircons crystallized and grown in the magma continuing from saturation to the solidus.

Conditions for Crystallization

Interior batholith plagioclase grains are most abundant with large subhedral to euhedral textures and surrounded by less well-developed quartz and microcline indicating a cooling over a large interval of time and temperature. The only plagioclase grains with inclusions within the cores are closed within one layer indicating inheritance as it includes zircon and apatite and are primarily in grains of samples nearest to the magma-wall rock interface. Subhedral-euhedral biotite followed closely behind, forming along boundaries indicating a higher H_2O content of the magma at earliest stages. Boundaries of the biotite grains show evidence of chloritization. Amphibole and oxides crystalized next into glomerocrysts – a porphyritic texture of clustered phenocrysts into aggregates, or clumps. A large cooling interval is supported further by the occurrence of epidote replacing amphibole (hornblende). Quartz and microcline finish out the sequence in sub to anhedral grains. Pervasive alteration of plagioclase to sericite occurs after the solidus. Glomerocrysts of amphibolite and oxides demonstrate boundaries indicative of xenocrystic inclusions which occur regularly during assimilation.

Core analyses represent the inherited mass of zircon with Precambrian ages from wall rock melting. Meanwhile, younger Eocene aged rims represent new crystallization in the magma. The statistical percentage of cored zircons within ages of the wall rock versus the magmatic age cores was expected to represent the volume of magma affected by wall rock melting due to the resistance of zircon crystals as being crucial in determining inheritance. However, inheritance is minimal in the granite and is not as informative as originally hypothesized. The notable result concludes that zircon in the granitoids is relatively uniform in age but are younger than suggested by Mills and Coleman (2013). Whereas host rock zircons show partial resetting with a massive discordance in age pick representing the volume of affected material at the boundary during storage. The age of the zircon is not suggested, but rather the intercepts of Concordia show more appropriate and consistent ages for heating and age of crystallization. Though different from Mill et al. (2013) they are still reasonable and demonstrate the evolution of zircon mineral grains in solution. There is a significant volume of wall rock melting and recrystallizing in the intruding pluton over time indicated by the range in Precambrian ages in inherited cores, despite the abundance of these being fewer than was expected. It is suggested that rim to core relationship must be further constrained by rerunning all the samples to determine if the core of the grains was truly reached by the laser, or if a mantle layer was being analyzed as indicated by the mixed ages. Interior samples show multiple provenance ages for zircon. One hundred forty zircons from the interior yield ages between 32-35 Ma and 113 zircon yield ages of ~35 Ma indicating primary crystallization. Two hundred twenty-four zircons of the interior zircons yielded an age between 35-50 Ma indicating inheritance from the magma with an antecrystic origin without dissolution. Only 19 zircons yielded ages greater than 50 Ma suggesting only a small number of zircons were inherited from either the magmatic source or the intruded country

rock. At 50 Ma, magmatism related to the end of the Laramide had ceased suggesting older zircon ages indicate partial melting of the magmatic source and subsequent inheritance or partial resetting during magma generation. Inheritance through the interface is unlikely in large amounts and is also not likely in abundance from the interior (i.e., MTP-1).

Zircon Age Corresponding to Growth Versus Dissolution

The range in crystallization ages observed in Mt. Princeton zircon are within error for each transect and do not suggest that weighted mean ages are inaccurate. Interior samples recorded MSWD ~ 0.64 - 3.2 with an average of 1.87, indicating that one or more sources of uncertainty are underestimated causing a slight over dispersion. This is most likely due to underestimating the amount of Precambrian aged cores in the zircon. The MSWD nearing a value of just above one indicates only a slight overdispersion and could be closer if more grains were omitted. The spread of U-Pb zircon ages and the error associated with each sample, increases as distance increases from the magma-wall rock interface (Fig. 3). This is expected if there were to be crystallization occurring through inheritance from the source as crystals terminate growth. Olierook et al. (2020) suggests $Th_{(Zirc\text{-}WR)}/U_{(Zirc\text{-}WR)}$ ratio can be used to differentiate autocrystic versus xenocrystic and restitic zircon grains. Autocrystic zircon plot between the calculated zircon-melt equilibrium curve and record Th/U fractionation trend with high correlation coefficient towards lower $Th_{(Zirc\text{-}WR)}/U_{(Zirc\text{-}WR)}$. Inherited or antecrystic zircon plot above this curve indicating they crystallize in disequilibrium with the melt and potentially higher temperatures (Kirkland et al., 2015). Both xenocrystic and antecrystic zircons are expected to be in significant disequilibrium with the silicate melt which they reside, regardless of how they were incorporated and given the timescales of magma generation, emplacement and

crystallization, and the rates of diffusion for both U and Th in zircon, diffusional equilibration is expected to be negligible (Cherniak et al., 1997). Furthermore, xenocrytstic grains inherited prior to magma emplacement are expected to record the composition of the zircon source and their primary melt. Whole rock and zircon fractional crystallization regressions through compared to xenocrystic grains show poor overlap and low correlation coefficients whereas, antecrystic zircon may show some overlap with zircon crystallized in the melt. Xenocrystic and restitic grains in the batholith are in low abundance, as most of the zircon grains are in equilibrium with the melt. The samples that contain zircon in disequilibrium of Th/U with the melt are located closer in proximity to the interface and are therefore inherited from the much older Precambrian wall-rock (Fig. 4).

Crystal-melt Heterogeneity and Magma Differentiation Revealed by Zircon Trace Elements

Trace element signatures recorded in igneous zircon have been suggested as a useful tool to track the magmatic evolution processes of the host rock (Yan et al., 2020). Trace element in zircon crystallized over a wide range of mafic to granitic compositions are in equilibrium with the melt during crystallization suggesting that changes in zircon trace element composition both within a single grain and between grains reflect the evolution of the melt (Claiborne et al., 2010; Deering et al., 2016; Wu et al., 2022). Hafnium contents and Gd/Yb ratios are commonly used as monitors of melt evolution where high Hf content and low Gd/Yb ratios in zircon correspond to growth in a relatively evolved melt (Klemetti and Clynne., 2014; Rentz et al., 2019).

Grimes et al. (2007, 2015), Kirkland et al. (2015) and Carley et al. (2014) identified compositional fields for zircon formed in silicic rock, specifically granitoids and rhyolites, from

a range of tectonic-magmatic environments based on Hf, U, REE, and Th/U ratios. Klemetti and Clynne (2014) added magmatic storage conditions based on Ti-in-zircon temperature, Hf content and Eu anomaly. When plotted in these fields' zircons from the Mt. Princeton Batholith generally records a continental adiabatic melting signature with MORB to arc source (Fig. 13; Carley et al., 2014). The Precambrian wall rock zircons show a more transitional continental signature between arc and MORB U/Yb and Gd/Yb zircon signatures (Fig. 13). Hafnium contents from both the batholith and the wall rock are enriched compared to typical continental environments and suggest melting of a continental source. The geochemical variability between zircons is likely the consequence of partial melting of and assimilation between a homogeneous monzogranite and a wall rock prior to zircon saturation which resulted in a heterogeneous magma crystallizing the zircons. While not separated into distinct populations of zircons, individual trends are present in each transect.

Transect 1: There was <3% assimilation of the wall rock (Fig. 14 and Fig. 18) and 6.9% of zircons with Precambrian age cores were included in the granitic body indicating the volume of partial melting of the wall rock. It is worth note that assimilation is based on feldspar and whole rock modeling, whereas including the zircon included does not define, but rather models, the process. This is greater than the 3% assimilation and thus does not indicate chemical diffusion. Moreover, half of these zircon cores >50 Ma are from COT 2, the sample closest to the interface. This decreases to only an eighth of these cores for COT 6, 7 and 8 farther from the magma-wall rock contact.

Fractional crystallization and assimilation models for the potential compositional variation of zircon from the Mt. Princeton Batholith. U/Yb versus Hf content models show fractional crystallization of the granitoid and assimilation of the Precambrian host rock

surrounding the batholith. Zircon from transect 1 supports a mix of fractional crystallization and assimilation. Samples COT 8 and those farthest from the interface require little to nothing in the way of assimilation to produce U/Yb vs Hf of the zircon.

Transect 2: There was <3% assimilation of the wall rock and 4.7% of zircons with Precambrian age cores were included in the granitic body indicating the volume of partial melting of the wall rock (Fig. 15). This is greater than the 3% assimilation and thus does not indicate chemical diffusion. Three quarters of the >50 Ma cores are a part of COT 21 (the closest sample analyzed near the contact), a quarter of them are in COT 27, and none from COT 33. This also indicates influence from the contact decreasing as distance from the interface increases.

Fractional crystallization and assimilation models for the potential compositional variation of zircon from the Mt. Princeton Batholith as in transect 1. U/Yb versus Hf content in zircon models suggest fractional crystallization of the granitoid and assimilation of the Precambrian host rock surrounding the batholith. Zircon from transect 2 shows less fractional crystallization but a great number of samples support assimilation (those included in, on, or located in close proximity to the interface). A mix of the methods accounts for the U/Yb vs Hf of the zircon.

Crystal-scale K-Feldspar Trace Element and Sr Isotopic Heterogeneity

Trace element signatures in K-feldspar are used as a tool to determine and support behavior of a melt during the evolution of a magma system. Feldspar trace elements in equilibrium with the crystal melt suggests that the mineral grains reflect the stage of melt

evolution at which it resided. Sr values are used to do the same in this section (Davidson et. al., 2008).

Crystal-scale initial isotopic ratios ranges for the Mt. Princeton Batholith are variable with distance from the magma-wall rock interface and within a single sample location. Studies have investigated crystal-scale variation in Sr isotopes produced through mixing of magma batches where disequilibrium is measured through melting of metasedimentary sources (Farina et. al., 2014). In this study we investigated Sr variation at the crystal scale without the mixing equivalent and with a meta-granite source producing disequilibrium. Farina et. al. (2011) suggests Sr isotope variation is unavoidable during partial melting of the crust, including partial melting during dissolution and incorporation of the wall rock across the quenched boundary in this study (Fig. 12). Variability of $^{87}Sr/^{86}Sr$ at the crystal-scale retained original isotope variability, even at the oldest ages with Rb/Sr values over one (COT 14), because Sr-Spec resin chromatographic column technique removed Rb influence and returned data at the crystals' closure composition (Farina et. al., 2014).

Similar trends are present in both transects concerning Sr isotopic ratios and trace elements. Intra-rock $^{87}Sr/^{86}Sr$ is in disequilibrium with whole rock ratios for the melt. This demonstrates an open system dissolution during partial melting of the wall-rock rather than the source melt. COT 14 of the Precambrian wall-rock and COT 27 and 33 of the interior granitoid demonstrate this relationship. The mineral Sr isotopic ratio is larger than the whole rock Sr. Though Precambrian $^{87}Sr/^{86}Sr$ is lower in transect 1 than transect 2, the positive trend of Sr to Ba and the disequilibrium of intra-rock to whole rock $^{87}Sr/^{86}Sr$ is similar. This also supports an open system with the <3% assimilation of the wall-rock (Fig. 16).

Magma Fluxes in the Mt. Princeton Batholith

These data provide indications of mineral-melt disequilibrium and were used to evaluate the pressure, temperature, and otherwise the range of intensive parameters surrounding emplacement and storage of the intrusive magma body. The foremost technique to understanding the ratio of inherited mineral phases to those that are magmatic in origin involves evaluating in situ crystal studies coupled with detailed petrography to resolve variations in the dynamics of intrusive magmatic systems (Davidson et al., 2008).

The variation of Sr/Sr from the metamorphic wall-rock to the interior is due to the parental magmatic source in the lower crust - likely a stable garnet source's signature. During the silicic material's accension in the crust to the position in which it feeds the caldera prior to eruption of the CCVF, zircon antecrysts were introduced at 820˚C according to the zircon process vs. temperature (Fig. 11). The magmatic body emplaced shallowly, at 6km, indicated by hornblende temperatures forming a quenched margin, indicated by the moderately limited radius of diffusion across the interface of the interior and the wall-rock. This is supported by the spread in ages and their error as distance increases from the interface. The assimilation of the wall rock occurred at the quenched boundary and affected roughly 3% of the Precambrian crustal material as supported by partial resetting of ages in zircon from the exterior of the batholith and $^{87}Sr/^{86}Sr$ of K-feldspar.

IMPLICATIONS

The proposed model offers perspectives on the behavior of silicic granitic composition magmas intruding upon like composition metamorphic rocks of the crust. These data demonstrate the decrease in crustal influence as distance increases away from the interface of the magma-wallrock. During interactions of similar composition magma to the crust it intrudes upon, it seems the crustal melt affects the system the least with a great deal of the variation in composition coming from the source. A principal implication of this study is that isotopic variation and mineral composition behave more similarly to a closed system when like-composition magma interacts with the crust. It would prove to be useful in areas of comparable environment such as the Sierra Nevada for studies that investigate magma emplacement and behavior. Based on the data presented here the following considerations need to be made will considering the compositional variability on epizonal and compositionally heterogeneous granitoids:

1. Whole rock trace element and Sr and Pb isotope ratios, zircon U-Pb ages and trace element contents, and K-feldspar trace element and isotopic data suggest that localized contamination occurs only at the wall rock-magma interface and only occurs early in magma crystallization. No significant assimilation of the Precambrian wall rock occurred during the emplacement of the Mt. Princeton Batholith.
2. Zircon trace element data suggests that at the magma wall rock interface, zoned zircon crystal reflect the magma crystallization and evolution history rather than the incorporation of xenocrystic cores. This suggests that even at the short time periods of magma storage observed at the wall rock-magma interface that zircons only record a portion of the magmatic history and a significant amount of time of magma storage was above zircon saturation temperatures.
3. The proposed model of magma-wall rock interaction expands the numerical models of Farina et al. (2012; 2014) on the extent of 87Sr/86Sr mineral scale variability in granitoid magmas by requiring knowledge of the thermal state of the crust source and wall rock composition. Magmas stored “cold” intruding and interacting with cold or similar temperature wall rock does not provide energy needed for extraction of partial melt in the wall rock and do not create mineral-scale isotopic variability.

REFERENCES

Brock, M. R., and Barker, F., 1972, Geologic Map of the Mount Harvard Quadrangle, Chaffee and Gunnison Counties, Colorado: map, Department of the Interior United States Geological Survey.

Carley, T.L., Miller, C.F., Wooden, J.L., Abraham, J.P., Schmitt, A.K., Economos, R.C., Bindeman, I.N., and Brennan, T.J., 2014, Iceland is not a magmatic analog for the Hadean: Evidence from the zircon record: Elsevier, Earth and Planetary Science Letters, v. 405, p. 85-97, doi: 10.1016/j.epsl.2014.08.015.

Cherniak D.J., Hanchar J.M., Watson E.B., 1997, a Diffusion of tetravalent cations in zircon: Contributions to Mineralogy and Petrology, v. 127, p. 383-390.

Claiborne, L., Miller, C.F., and Wooden, J.L., 2006, Trace element composition of igneous zircon: A thermal and compositional record of the accumulation and evolution of a large silicic batholith, Spirit Mountain, Nevada: Contributions to Mineralogy and Petrology, v. 160, p. 511-531, doi: 10.1007/s00410-010-0491-5.

Coleman, D.S., Gray, W., and Glazner, A.F., 2004, Rethinking the emplacement and evolution of zoned plutons: Geochronologic evidence for incremental assembly of the Tuolumne Intrusive Suite, California: Geological Society of America, v. 32, no. 5, p. 433-436, doi: 10.1130/G20220.1.

Davidson, J.P., Font, L., Charlier, B.L.A., and Tepley III, F.J., 2008, Mineral-scale Sr isotope variation in plutonic rocks– a tool for unravelling the evolution of magma systems: Proceeding of the Royal Society of Edinburgh, v. 97, p. 357-367.

Deering, C.D., Keller, B., Schoene, B., Bachmann, O., Beane, R., and Ovtcharova, M., 2016, Zircon record of the plutonic-volcanic connection and protracted rhyolite melt evolution: The Geological Society of America, doi: doi:10.1130/G37539.1.

Ferry J.M., and Watson E.B., 2007, New thermodynamic models and revised calibrations for the Ti-in-zircon and Zr-in-rutile thermometers: Contributions to Mineralogy and Petrology, v. 154 p. 429-437.

Harrison T.M., Watson E.B., and Aikman A.B., 2007, Temperature spectra of zircon crystallization in plutonic rocks: Geology, v. 35 (7) p. 635-638.

Hayden L.A., and Watson E.B., 2007, Rutile saturation in hydrous silicate melts and its bearing on Ti-thermometry of quartz and zircon: Earth and Planetary Science Letters, v. 258 p. 561-568.

Jarosewich, E., 2002, Smithsonian Microbeam Standards: Journal of Research of the National Institute of Standards and Technology, v. 107, p. 681-685, doi:10.6028/jres.107.054.

Kay, S.M., Coira, B.L., Caffe, P.J., and Chen C., 2010, Regional chemical diversity, crustal and mantle sources and evolution of central Andean Puna plateau ignimbrites: Journal of Volcanology and Geothermal Research, v. 198 p. 81-111.

Klemetti, E.W., and Clynne, M.A., 2014, Localized Rejuvination of a Crystal Mush Recorded in Zircon Temporal and Compositional Variation at the Lassen Volcanic Center, Northern California: PLoS ONE 9(12): e113157. doi:10.1371/journal.pone.0113157.

Lipman, P.W., 2007, Incremental assembly and prolonged consolidation of Cordilleran magma chambers: Evidence from the Southern Rocky Mountain volcanic field: Geosphere, v. 3, p. 42-70, doi: 10.1130/GES00061.1.

Liu, Y., Hu, Z., Gao, S., Gunther, D., Xu, J., Gao, C., and Chen, H., 2008, In situ analysis of major and trace elements of anhydrous minerals by LA-ICP-MS without applying an internal standard: Chemical Geology, v. 257, no. 1-2, p. 34-43, https://doi.org/10.1016/j.chemgeo.2008.08.004.

Ludwig, K.R., 2003, Mathematical-statistical treatment of data and errors for Th-230/U geochronology: Uranium-Series Geochemistry, Reviews in Minerology and Geochemistry, v. 52, p. 631-656.

McDowell, S.M., Miller, C.F., Mundil, R., Ferguson, C.A., and Wooden, J.L., 2014, Zircon evidence for a ~200 k.y. supereruption-related thermal flare-up in the Miocene southern Black Mountains, western Arizona, USA: Contributions to Mineralogy and Petrology, 167:1031 doi 10.1007/s00410-014-1031-5.

McItosh, W.C. and Chapin, C.E., 2004, Geochronology of the central Colorado volcanic field: New Mexico Bulletin of Geology and Mineral Resources Bulletin, p. 205-211.

McLeod, C.L., Davidson, J.P., Nowell, G.M., and de Silva, S.L., 2012, Disequilibrium melting during crustal anatexis and implications for modeling open magmatic systems: Geology, v. 40, no. 5, p. 435-438.

Michelfelder, G.S.; Feeley, T.C.; Wilder, A.D., and Klemetti, E.W., 2013, Modification of the continental crust by subduction zone magmatism and vice-versa: across-strike geochemical variations of silicic lavas from individual eruptive centers in the Andean Central Volcanic Zone: Geosciences, v. 3, p. 633-667.

Mills, R.D. and Coleman D.S., 2013, Temporal and chemical connections between plutons and ignimbrites from the Mount Princeton magmatic center: Contributions to Mineralogy and Petrology.

Mills, R.D., Glazner, A.F., and Coleman D.S., 2009, Scale of pluton/wall interaction near May Lake, Yosemite National Park, CA, USA: Contributions to Mineralogy and Petrology.

Olierook, H. K. H., Kirkland, C. L., Szilas, K., Hollis, J.A., Gardiner, N. J., Steenfelt, A., Jiang, Q., Yakymchuk, C., Evans, N. J., and McDonald, B. J., 2020, Differentiating between Inherited and Autocrystic Zircon in Granitoids: Journal of Petrology, v. 61, no. 8, p. 1-22, doi: 10.1093/petrology/egaa081.

Paton, C., Hellstrom, J., Bence, P. Woodhead, J., Hergt. J., 2011, Iolite: Freeware for the visualisation and processing of mass spectrometric data: Journal of Analytical Atomic Spectrometry, v. 26, no. 12, p. 2508-2518. doi: 10.1039/C1JA10172B.

Ramos, F.C., and Reid, M.R., 2005, Distinguishing melting of heterogeneous mantle sources from crustal contamination: Insights from Sr isotopes at the phenocryst scale, Pisgah Crater, California: Journal of Petrology, v. 46, p. 999-1012.

Rentz, S.P., Michelfelder, G., Coble, M.A., and Salings, E., 2018, U-Pb zircon geochronology of calc-alkaline ash flow tuff units in the Mogollon Datil Volcanic Field, southern New Mexico: Geological Society of America Special Paper, v. 528, p. 409-434.

Ridolfi, F., Renzulli, A., and Puerini, M., 2010, Stability and chemical equilibrium of amphibole in calc-alkaline magmas: an overview, new thermobarometric formulations and application to subduction-related volcanoes: Contributions to Mineralogy and Petrology, v. 160, p. 45-66.

Ridolfi, F., Renzulli, A., 2012, Calcic amphiboles in calc-alkaline and alkaline magmas: thermobarometric and chemometric empirical equations valid up to 1130◦C and 2.2 GPa: Contributions to Mineralogy and Petrology, p. 163, v. 877-895.

Shannon, J.R., 1988, Geology of the Mount Aetna cauldron complex, Sawatch Range, Colorado [Ph.D. thesis]: Colorado School of Mines, Colorado, p. 439.

Sommer, S., Bohannon, L., and Michelfelder, G.S., 2022, U-Pb Geochronology of Titanite and Zircon to Date Metamorphic Reset of 1.6 Ga Metamorphic Plutonic Rocks Near Buena Vista, Colorado: Geological Society of America Abstracts with Programs, v. 54, No. 4, 2022, doi: 10.1130/abs/2022NC-374479.

Tepley III, F.J., Davidson, J.P., Tilling, R.I., and Arth, J.G., 2000, Magma mixing, recharge and eruption histories recorded in plagioclase phenocrysts from El Chichòn Volcano, Mexico: Journal of Petrology, v. 41, no. 9, p. 1397-1411.

Todt, W., Cliff, R.A., Hanser, A., and Hofmann, A.W., 1996, Evaluation of a 202Pb-205Pb Double Spike for High-Precision Lead Isotope Analysis. In Earth Processes: Reading the Isotope Code; Hart, S.R., Basu, A., Eds.; American Geophysical Union: Washington, DC, USA, v. 95, p. 429-437.

Watson E.B., and Harrison T.M., 2005, Zircon thermometer reveals minimum melting conditions on earliest Earth: Science v. 308, p. 841-844.

Watson E.B., Wark D.A., and Thomas J.B., 2006, Crystallization thermometers for zircon and rutile: Contributions to Mineralogy and Petrology, v. 151, v. 413-433.

Woodhead, J., and Hergt, J., 2007, A Preliminary Appraisal of Seven Natural Zircon Reference Materials for In Situ Hf Isotope Determination: Geostandards and Geoanalytical Research, v. 29, no. 2, p. 183-195.

Wu, J., Rowe, M.C., Cronin, S.J., Wolff, J.A., and Fu, B., 2022, Long-lived dacitic magmatic systems and recharge dynamics in the Jemez Mountains volcanic field, western USA:

Contributions to Mineralogy and Petrology, v. 177:62, p. 1-17, doi: 10.1007/s00410-022-01930-9.

Yan, L., and Beier, C., 2020, Tracking crystal-melt segregation and magma recharge using zircon trace element data: Chemical Geology, doi:10.1016/j.chemgeo.2020.119596.

Zimmerer, M.J., and McIntosh, W.C., 2012, An investigation of caldera-forming magma chambers using the timing of ignimbrite eruptions and pluton emplacement at the Mt. Aetna caldera complex: Journal of Volcanology and Geothermal Research, v. 245-246, p. 128-148.

FIGURES AND TABLES

Table 1. U/Pb zircon geochronology separated by interior and exterior of the pluton. Values are averages of grains for each sample.

Sample ID	n	U/Th Ratio	$^{206}Pb/^{238}U$	Error (%)	$^{207}Pb/^{235}U$	Error (%)	$^{207}Pb/^{206}Pb$	Error (%)	Ages (Ma)				concordia age	MSWD
									$^{206}Pb/^{238}U$	Error (Ma)	$^{207}Pb/^{235}U$	$^{207}Pb/^{206}Pb$		
Precambrian Host Unit														
COT - 3	12	16.092	0.162	0.005	2.275	0.134	0.067	0.056	937.000	26.333	1080.667	58.000	765.60 ± 7.04	
COT - 14	72	10.648	0.157	0.006	2.461	0.163	0.123	0.014	932.478	34.672	1171.358	40.507	924.51 ± 1.15	0.04
Interior														
COT - 2	83	1.438	0.009	0.000	0.432	0.030	0.123	0.011	54.879	2.607	177.310	9.376	34.990 ± 0.053	0.03
COT - 4	58	1.817	0.005	0.000	0.055	0.006	0.072	0.008	35.263	1.100	53.702	5.400	35.167 ± 0.063	0.05
COT - 6	48	1.402	0.008	0.001	0.079	0.012	0.062	0.006	48.001	4.102	62.054	7.723	35.300 ± 0.073	0.02
COT - 7	38	1.833	0.011	0.001	0.232	0.021	0.082	0.007	68.917	5.252	120.276	9.837	35.719 ± 0.085	0.03
COT - 8	24	1.533	0.008	0.000	0.314	0.029	0.107	0.010	49.920	2.753	145.871	11.229	35.32 ± 0.10	0.02
COT - 21	14	1.578	0.009	0.001	0.346	0.037	0.140	0.014	59.274	4.416	186.029	14.421	34.94 ± 0.16	0.02
COT - 27	40	1.772	0.006	0.001	0.067	0.014	0.067	0.008	40.968	3.016	57.548	8.853	35.195 ± 0.082	0.01
COT - 33	37	2.008	0.006	0.000	0.057	0.007	0.072	0.009	35.614	1.440	54.019	6.006	35.12 ± 0.10	0.03
Precambrian Lens														
COT - 30	45	15.316	0.153	0.006	2.107	0.115	0.102	0.007	912.156	36.067	1112.956	38.822	1019.48 ± 1.67	0.03
Border Unit														
COT - 15	25	7.322	0.100	0.005	1.525	0.103	0.112	0.004	602.768	26.224	861.552	32.324	437.61 ± 1.23	0.23

n = number of zircons grains analyzed per sample

MSWD ~ 1.0 accepted. High MSWD reject concordia age and suggest more appropriate intercept ages.

Table 2. Average trace element content in zircon.

Sample ID	Sc (ppm)	Ti (ppm)	Y (ppm)	Nb (ppm)	La (ppm)	Ce (ppm)	Pr (ppm)	Nd (ppm)	Sm (ppm)	Eu (ppm)	Gd (ppm)
Precambrian Host Unit											
COT - 3	110.87	606.22	591.37	1.9023	0.14	7.0578	0.0969	1.2656	2.5211	0.401	13.051
COT - 4	136.42	603.17	675.47	2.9534	34.305	82.651	6.4015	24.075	5.7962	1.0504	15.004
COT - 14	128.06	697.11	2457.1	2.5706	659.75	2691.2	475.59	2293.8	750.28	18.575	687.98
Interior											
COT - 2	137.69	720.57	1527.3	3.9828	5366	7849.4	595.47	1765.1	210.38	22.587	193.53
COT - 6	127.44	636.67	628.8	2.9012	12.152	44.588	2.0427	8.6231	3.7947	0.9186	13.979
COT - 7	130.64	580.4	602.67	3.204	1.6993	25.245	0.3079	1.9857	2.5467	0.7556	12.265
COT - 8	113.13	624.93	1007.6	3.082	5173.9	7614.2	584.23	1694.6	178.02	26.486	153.67
COT - 21	129.82	681.57	805.79	2.9938	3833	5233.6	342.87	930.1	88.251	13.827	92.338
COT - 27	137.05	619.89	644.44	2.4153	54.606	91.231	5.7771	17.967	4.3644	0.9744	14.078
COT - 33	128.14	895.5	580.89	2.9698	5.5615	29.069	0.8156	3.794	2.5282	0.6259	11.223
Precambrian Lens											
COT - 30	119.12	566.88	246.07	2.5692	1.4243	6.8516	0.621	3.0212	1.7143	0.426	6.0015
Border Unit											
COT - 15	142.92	618.53	2757.3	32.945	4.0129	16.6	2.2271	15.208	15.34	2.641	55.063

Sample ID	Tb (ppm)	Dy (ppm)	Ho (ppm)	Er (ppm)	Tm (ppm)	Tb (ppm)	Lu (ppm)	Hf (ppm)	Ta (ppm)	Th (ppm)	U (ppm)
Precambrian Host Unit											
COT - 3	4.6076	55.563	20.498	94.178	20.207	191.01	31.718	4543.1	0.8566	57.114	121.73
COT - 4	4.5914	54.294	21.002	105.77	24.719	260.64	50.478	5715.7	1.0561	286.23	443.09
COT - 14	90.612	490.39	92.094	246.44	31.894	220.73	31.652	4678.2	1.1624	58.082	462.13
Interior											
COT - 2	25.24	176.14	49.536	201.68	40.088	372.51	70.537	5309.1	0.9128	571.48	434.16
COT - 6	4.5848	54.473	20.115	97.46	21.991	223.42	41.553	5477.3	0.9831	257.47	300.89
COT - 7	4.1727	50.433	19.417	92.553	22.025	229.13	40.938	5164.7	0.9358	261.17	330.84
COT - 8	17.75	114.53	30.728	123.82	24.927	245	46.011	4962.1	0.9909	463.11	379.74
COT - 21	11.182	83.05	26.081	111.18	23.753	236.81	41.96	4632.6	0.9703	306.73	337.8
COT - 27	4.3812	51.85	19.978	99.789	23.377	250.3	51.646	5853	0.7795	276.97	424.01
COT - 33	3.8736	48.132	18.881	92.236	21.891	228.07	43.896	5664.5	0.9628	253.26	312.93
Precambrian Lens											
COT - 30	1.9042	22.278	8.1115	38.37	8.8785	92.773	15.593	4981.5	1.4471	37.423	412.46
Border Unit											
COT - 15	20.797	243.64	86.362	409.81	93.945	934.56	166.77	6531	16.637	830.17	2432.8

Table 3. Average trace element content in K-feldspar.

Sample ID	Mg (ppm)	Ca (ppm)	Ca44 (ppm)	Fe (ppm)	Rb (ppm)	Sr (ppm)	Cs (ppm)	Ba (ppm)	La (ppm)	Ce (ppm)	Pr (ppm)	Nd (ppm)	Sm (ppm)	Eu (ppm)
Precambrian Host Unit														
COT - 14	4.07	1766.1	1736.8	547.5	104.32	199.71	0.2491	2094.6	0.3908	0.4745	0.0359	0.0927	0.0171	0.4155
Interior														
COT - 2	51.401	1427.2	1280.6	527.08	89.263	315.33	0.9467	2354.7	0.5124	0.4463	0.0316	0.0827	0.0367	0.3762
COT - 6	39.868	2623.3	2474.7	594.75	109.18	324.96	1.2085	2691.9	0.5867	0.3284	0.019	0.04	0.0081	0.3298
COT - 8	9.7382	2880.5	4209.7	676.1	99.11	325.26	0.7997	3913.5	0.697	0.4534	0.0181	0.034	0.0133	0.4481
COT - 21	2.0675	1462.3	1304.8	723.67	115.93	324.17	0.6532	3242	0.6622	0.3731	0.0168	0.0263	0.0068	0.4285
COT - 27	17.56	3753.5	3327.9	918.45	97.583	329.63	0.6131	3382.3	1.4325	1.0985	0.0632	0.131	0.0109	0.5416
COT - 33	25.653	13597	12623	1297	57.37	351.6	0.3228	1360.8	2.6965	2.6123	0.1915	0.5231	0.0555	0.4126
Border Unit														
COT - 15	649.47	8493.1	8051.9	6785.3	91.256	49.688	3.6149	183.51	0.9573	1.9343	0.2944	1.9668	0.8146	0.222

Sample ID	Gd (ppm)	Tb (ppm)	Dy (ppm)	Ho (ppm)	Er (ppm)	Tm (ppm)	Yb (ppm)	Lu (ppm)	Pb204 (ppm)	Pb206 (pm)	Pb207 (ppm)	Pb208 (ppm)	Th (ppm)	U (ppm)
Precambrian Host Unit														
COT - 14	0.0613	0.0021	0.0123	0.0032	0.0067	0.0038	0.0381	0.0024	16.832	15.768	15.462	15.243	0.0069	0.0816
Interior														
COT - 2	0.0638	0.0152	0.0201	0.0075	0.0117	0.0082	0.0909	0.0105	18.867	19.234	18.292	18.937	0.6188	2.7182
COT - 6	0.0716	0.0022	0.0129	0.006	0.0064	0.0133	0.0173	0.0016	21.692	21.926	20.714	21.908	0.191	0.1362
COT - 8	0.0881	0.0015	0.0121	0.0029	0.0029	0.001	0.0094	0.0055	174.92	26.425	22.119	20.857	0.0166	0.0958
COT - 21	0.0793	0.003	0.0041	0.0012	0.0002	0.0005	0.0074	0.0007	18.167	17.933	17.142	17.679	0.0121	0.032
COT - 27	0.1309	0.0024	0.0089	0.0014	0.0027	0.0003	0.0158	0.0029	19.375	17.964	18.603	17.747	0.2957	0.0753
COT - 33	0.0618	0.0041	0.0125	0.0102	0.0042	0.0007	0.0389	0.001	67.445	13.015	12.624	12.554	0.077	0.0998
Border Unit														
COT - 15	1.0498	0.1908	1.0544	0.2074	0.5275	0.0673	0.3731	0.0674	16.325	15.79	12.808	14.45	0.3634	0.1272

Table 4. Mineral radiogenic isotopic ratios of Sr and Pb from K-feldspar.

Sample ID	n*	$^{87}Sr/^{86}Sr$	error	$^{84}Sr/^{86}Sr$	$^{206}Pb/^{204}Pb$	error	$^{207}Pb/^{204}Pb$	error	$^{208}Pb/^{204}Pb$	error
Precambrian Host Unit										
COT - 14a	128	0.72335	1.1E-05	0.05644	17.342	0.001	15.448	0.001	38.361	0.002
COT - 14b	160	0.72362	1.5E-05	0.05645	17.351	0.001	15.449	0.001	38.445	0.001
COT - 14c	128	0.72552	1.1E-05	0.05643	17.449	0.001	15.456	0.001	38.451	0.002
COT - 14d					17.435	0.001	15.456	0.001	38.656	0.002
Interior										
COT - 2a	132	0.70879	1.5E-05	0.05643						
COT - 2b	160	0.70879	2.9E-05	0.05648	17.840	0.001	15.516	0.001	38.111	0.002
COT - 6a	160	0.70997	1.8E-05	0.05644						
COT - 6b	160	0.70865	1.3E-05	0.05644	17.801	0.001	15.510	0.001	38.085	0.002
COT - 6c	105	0.70904	1.3E-05	0.05644						
COT - 6d	160	0.70869	1.4E-05	0.05671						
COT - 7a					17.904	0.004	15.516	0.003	38.161	0.008
COT - 7b	128	0.71215	1.3E-05	0.05641						
COT - 8a	128	0.70844	0.00002	0.0564	17.791	0.001	15.510	0.001	38.112	0.001
COT - 8b	80	0.70855	1.1E-05	0.05646						
COT - 21a	128	0.70883	1.5E-05	0.05643	17.808	0.001	15.511	0.001	38.107	0.002
COT - 21b	61	0.70895	0.00001	0.05642						
COT - 27a	128	0.70855	1.3E-05	0.05639	17.805	0.002	15.511	0.001	38.099	0.002
COT - 27b	96	0.71128	1.5E-05	0.05634						
COT - 33a	160	0.70826	1.4E-05	0.0565	17.812	0.001	15.511	0.001	38.103	0.002
COT - 33b	128	0.70832	1.3E-05	0.05645	17.800	0.001	15.506	0.001	38.079	0.002
MTP - 1	128	0.70808	1.1E-05	0.05644						
Precambrian Lens										
COT - 30	128	0.71853	1.7E-05	0.05642						

n* indicates number cycles during TIMS analysis

Table 5. Whole rock trace element contents.

Sample ID	45 Sc	85 Rb	88 Sr	89 Y	90 Zr	93 Nb	133 Cs	137 Ba	139 La	140 Ce	146 Nd	147 Sm	153 Eu	157 Gd
Precambrian Host Unit														
COT - 14	1.801	86.648	370.164	4.128	13.851	5.504	0.804	1044.55	28.539	49.174	15.523	2.322	0.848	1.577
COT - 3	11.19	76.535	433.234	60.888	28.332	26.353	4.791	1193.29	64.778	129.56	64.295	13.32	3.016	11.006
COT - 4	5.144	151.386	403.42	22.994	25.209	18.426	3.416	769.199	71.528	108.772	37.233	6.065	1.293	4.519
Interior														
COT - 2	9.776	108.63	503.68	28.225	30.292	20.715	2.493	808.823	49.884	95.57	40.117	7.132	1.553	5.213
COT - 6	5.7	114.697	527.446	18.107	18.787	9.606	2.505	791.831	41.443	82.867	29.995	4.936	1.297	3.672
COT - 7	5.395	114.021	374.291	21.564	43.219	39.506	1.995	865.123	59.241	97.253	36.539	5.988	1.419	4.456
COT - 8	7.534	114.529	490.201	24.464	23.291	14.28	1.963	770.555	59.72	102.792	40.148	6.602	1.477	4.836
COT - 21	7.15	117.525	482.784	23.48	25.114	9.881	2.637	835.016	53.225	94.75	37.61	6.348	1.532	4.674
COT - 27	6.023	110.307	482.629	22.615	22.228	16.273	2.205	723.479	51.169	94.141	37.522	6.303	1.47	4.636
COT - 33	6.978	113.436	492.222	22.179	21.938	19.638	2.072	741.996	50.863	90.652	35.775	6.035	1.436	4.397
MTP - 1	8.616	116.426	538.008	25.498	31.028	20.149	2.118	865.12	60.458	106.344	42.02	7.052	1.605	5.133
Precambrian Lens														
COT - 30	3.505	103.184	387.74	9.06	21.762	15.708	1.096	954.172	44.993	68.229	21.8	3.371	1.032	2.375
Border Unit														
COT - 15	2.451	141.517	106.277	57.331	61.859	11.378	3.048	522.991	78.035	148.838	66.333	13.748	1.103	10.386

Sample ID	159 Tb	163 Dy	165 Ho	166 Er	169 Tm	172 Yb	175 Lu	178 Hf	181 Ta	204 Pb	206 Pb	207 Pb	208 Pb	232 Th	238 U
Precambrian Host Unit															
COT - 14	0.202	0.756	0.149	0.389	0.056	0.233	0.029	0.29	4.841	12.703	11.791	12.093	12.329	6.287	0.351
COT - 3	1.837	10.786	1.989	5.043	0.565	4.331	0.523	0.727	3.204	8.216	7.973	8.021	8.181	6.518	0.733
COT - 4	0.647	3.545	0.661	1.93	0.233	2.105	0.272	0.996	2.647	17.689	16.865	17.169	17.094	26.723	4.927
Interior															
COT - 2	0.769	4.387	0.814	2.282	0.281	2.321	0.294	1.218	2.683	17.185	16.278	16.8	16.62	22.838	3.967
COT - 6	0.523	2.841	0.533	1.534	0.179	1.516	0.193	0.774	1.148	17.196	16.019	16.712	16.705	21.261	2.633
COT - 7	0.627	3.368	0.622	1.752	0.21	1.796	0.231	1.959	7.254	16.075	15.742	15.996	16.114	20.429	2.606
COT - 8	0.699	3.793	0.7	2.011	0.239	2.02	0.257	0.99	1.859	16.776	15.452	15.777	15.636	25.002	4.502
COT - 21	0.704	3.763	0.715	1.971	0.242	1.942	0.266	1.05	1.18	16.459	15.412	15.883	15.658	20.511	4.076
COT - 27	0.668	3.656	0.681	1.913	0.229	1.922	0.248	1.026	3.564	15.318	13.847	14.509	14.397	23.235	4.255
COT - 33	0.649	3.457	0.655	1.853	0.226	1.86	0.252	1.01	6.85	15.572	14.741	15.16	14.982	19.367	4.175
MTP - 1	0.73	3.965	0.74	2.037	0.25	2.133	0.275	1.265	8.854	16.921	15.521	16.055	15.988	21.474	4.397
Precambrian Lens															
COT - 30	0.409	1.422	0.361	0.782	0.178	0.594	0.185	0.263	5.443	13.938	13.75	13.749	13.991	10.5	1.28
Border Unit															
COT - 15	1.637	9.197	1.697	4.488	0.558	4.664	0.614	1.963	2.259	36.225	46.933	37.645	40.883	51.598	8.712

Table 6. Whole rock isotope ratios of Sr and Pb.

Sample ID	n	$^{87}Sr/^{86}Sr$	error	$^{84}Sr/^{86}Sr$	$^{206}Pb/^{204}Pb$	error	$^{207}Pb/^{204}Pb$	error	$^{208}Pb/^{204}Pb$	error
Precambrian Host Unit										
COT - 14	128	0.717808	0.000008	0.05643	17.766	0.001	15.470	0.001	38.793	0.002
COT - 15					17.901	0.001	16.050	0.001	43.055	0.001
Interior										
COT - 27	128	0.708297	0.000013	0.05641	17.965	0.001	15.522	0.001	38.305	0.002
COT - 33	124	0.708272	0.000009	0.05643	17.953	0.001	15.521	0.001	38.266	0.002
MTP - 1	128	0.708077	0.000011	0.05644	18.011	0.001	15.528	0.001	38.308	0.002
Precambrian Lens										
COT - 30	128	0.718533	0.000017	0.05642	18.65	0.001	15.571	0.001	38.582	0.002

n* indicates the number of cycles during TIMS analysis

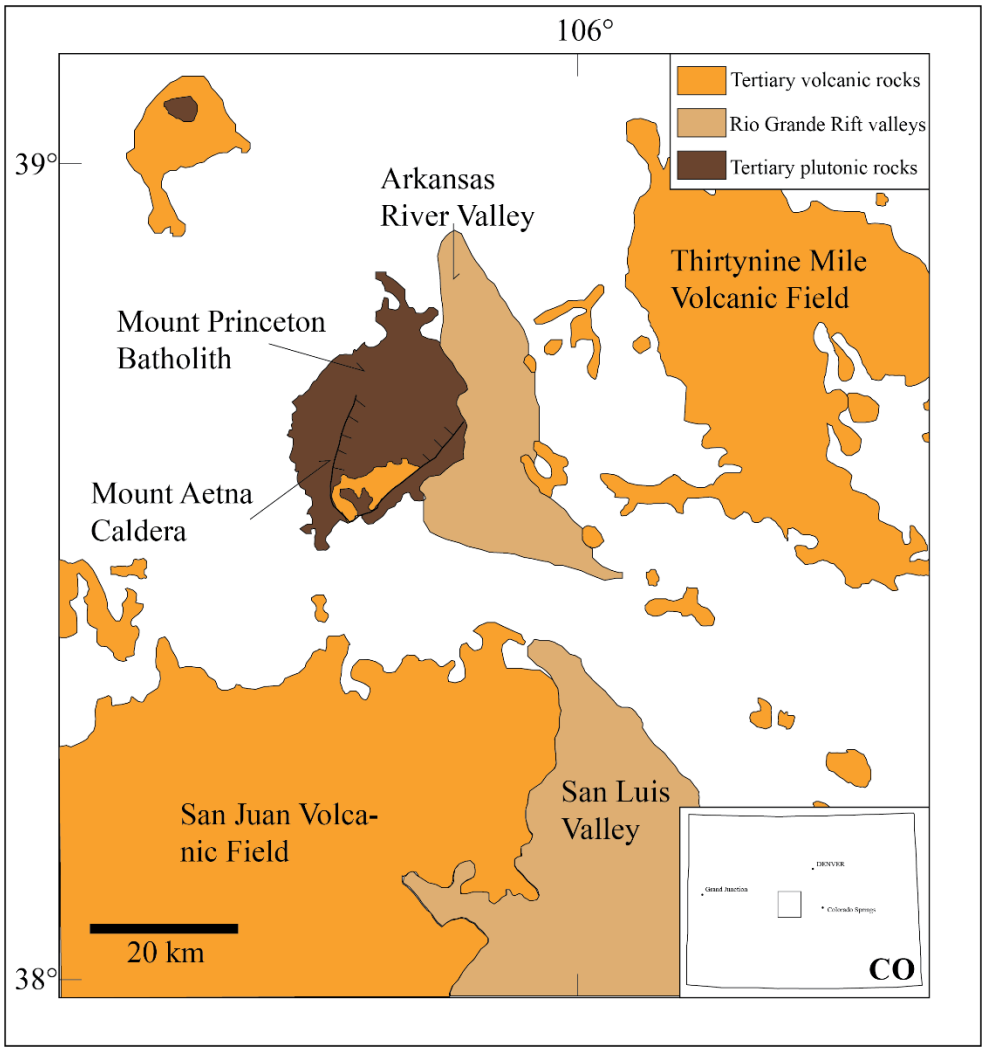

Figure 1. Overview map of central Colorado (modified from Mills and Coleman 2013 after McIntosh and Chapin, 2004) highlighting Tertiary plutonic and volcanic rocks notable and local rift valleys. Mt Princeton Batholith is shown in brown. Inset shows the location of the main figure within the state of Colorado.

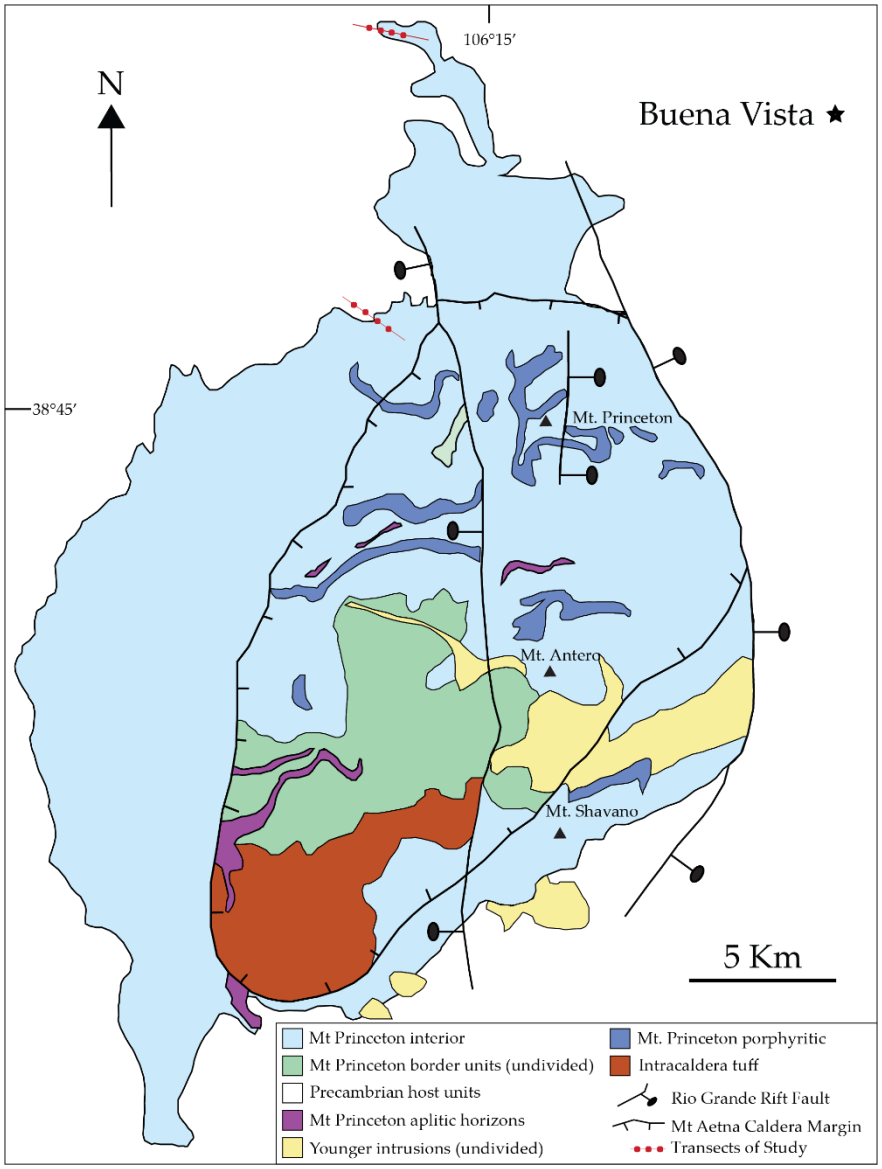

Figure 2. Simplified geologic map of Mt. Princeton Batholith (modified from Mills and Coleman, 2013 after Shannon, 1988) highlighting interior, exterior, and border units as well as transect locations for this study.

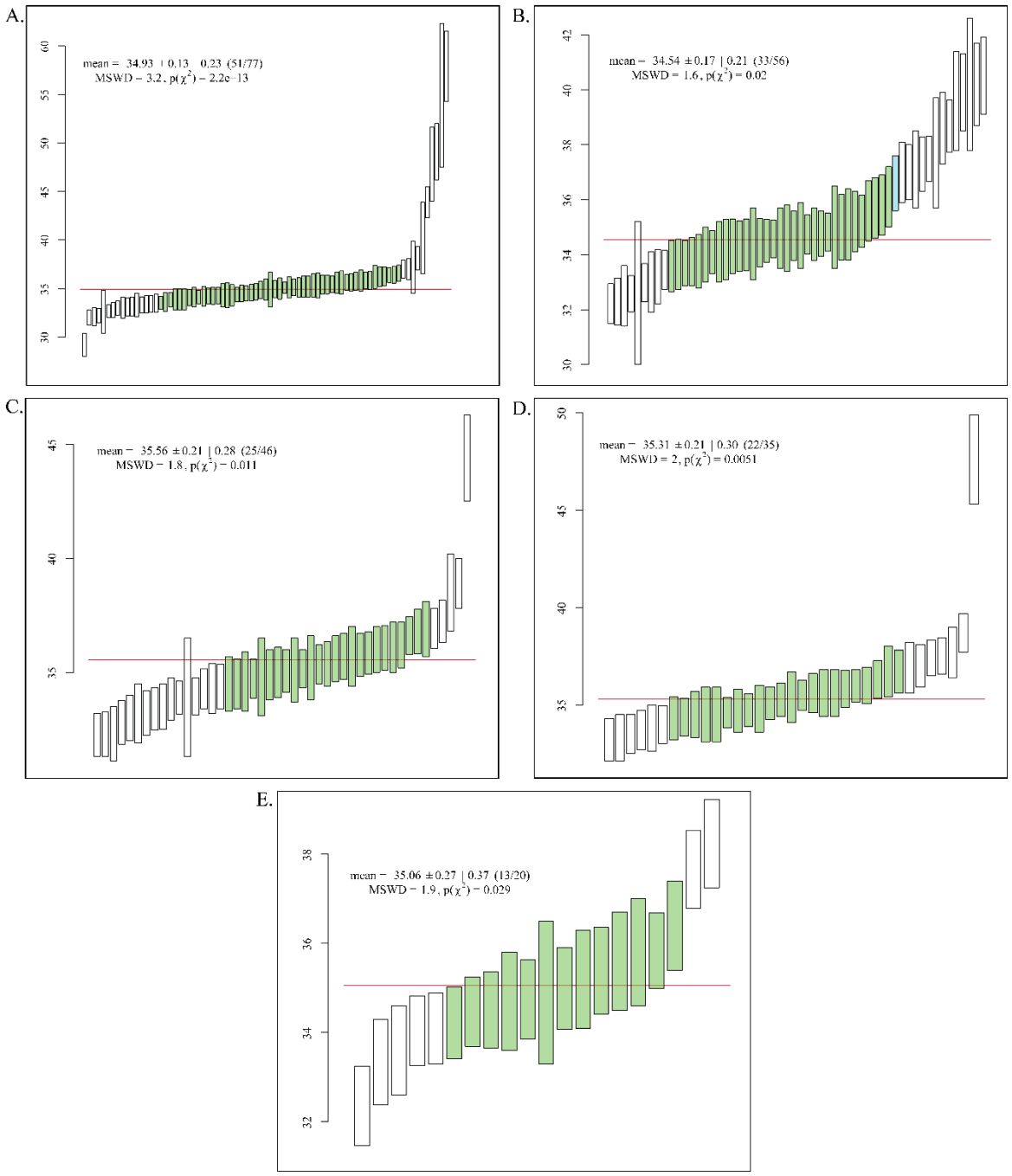

Figure 3. Zircon U-Pb weighted mean plots for samples from transect 1. Mean age and MSWD reported for each with green indicating selected grains, light blue representing outliers, and white showing omitted values. The red line indicates average age. Zircon ages were omitted based on criteria discussed in text. Sample COT3 only contained three zircon analyses and a weighted mean plot was not statistically significant. (A. COT 2, B. COT 4, C. COT 6, D. COT 7, E. COT 8).

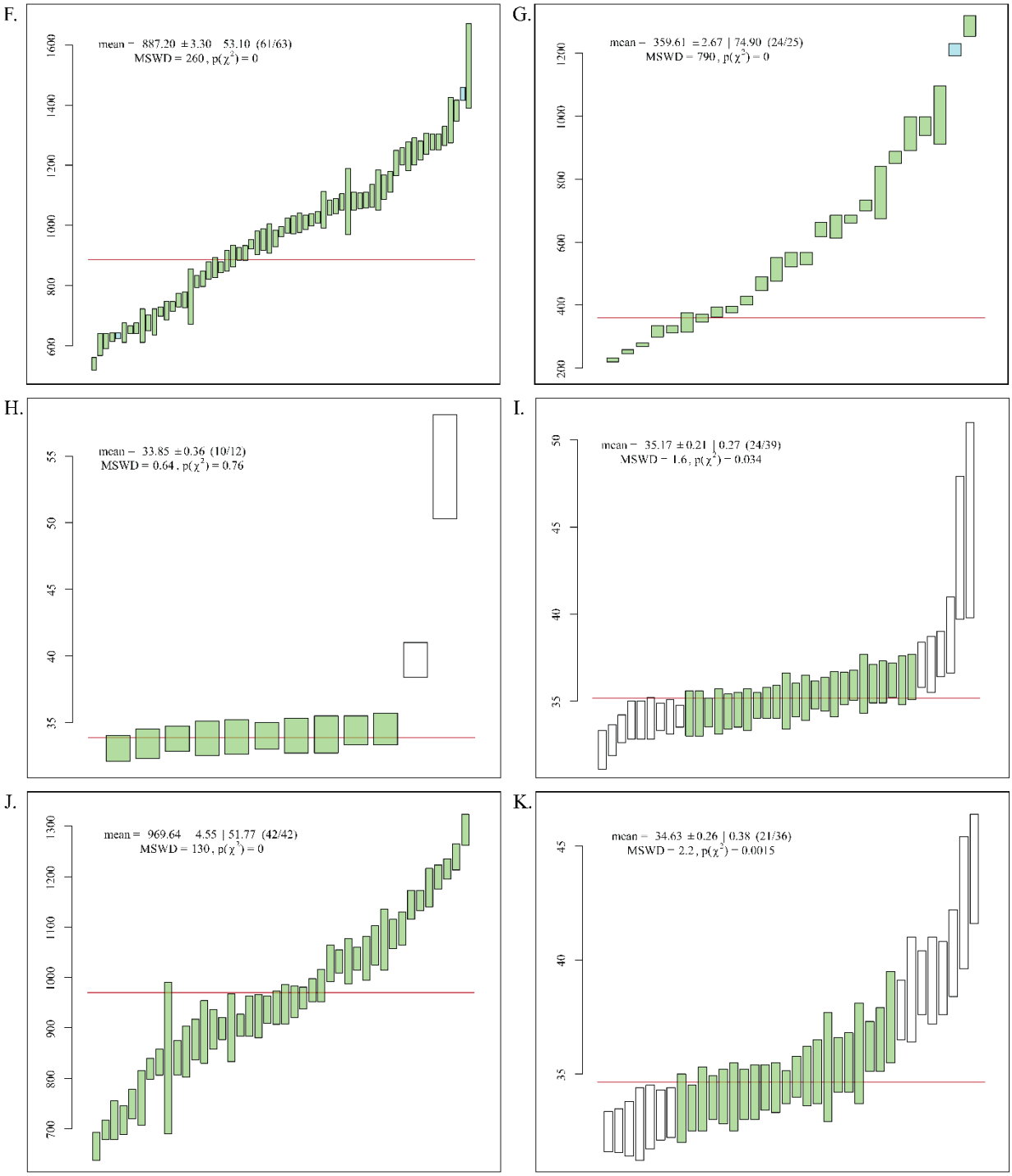

Figure 3 cont. Zircon U-Pb weighted mean plots for samples from transect 2. Mean age and MSWD reported for each with green indicating selected grains, light blue representing outliers, and white showing omitted values. The red line indicates average age. Zircon ages were omitted based on criteria discussed in text. Samples COT 14 and 15 represent the spread discussed in text for ages in Precambrian wall rock. Sample 30 is a lens of the Precambrian material from the crust. (F. COT 14, G. COT 15, H. COT 21, I. COT 27, J. COT 30, K. COT 33).

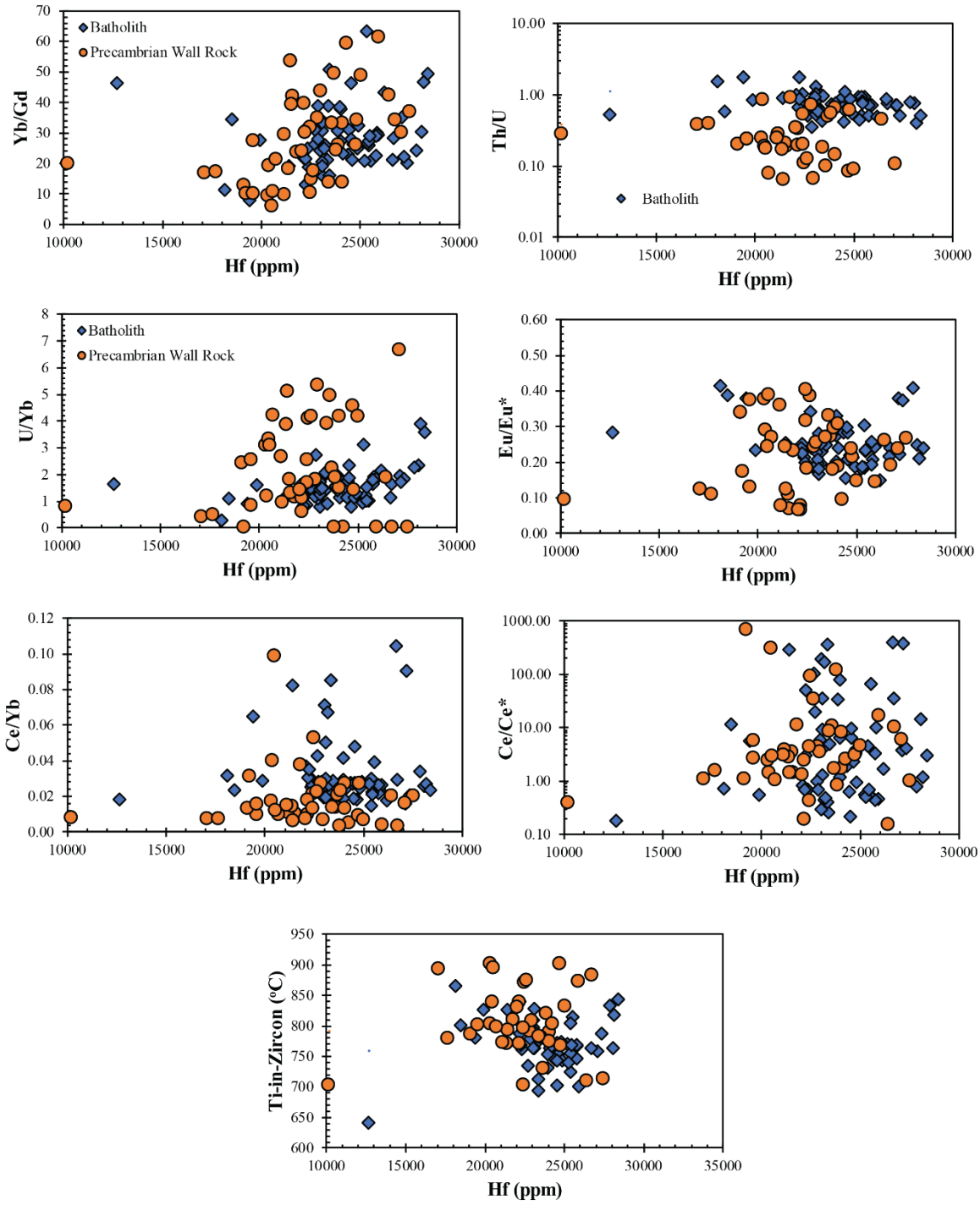

Figure 4. Bivariate trace element content and ratio plots of individual zircons: Yb/Gd versus Hf, Th/U versus Hf, U/Yb versus Hf, Eu/Eu* versus Hf, Ce/Yb versus Hf, Ce/Ce* versus Hf, and Ti-in-zircon°C versus Hf.

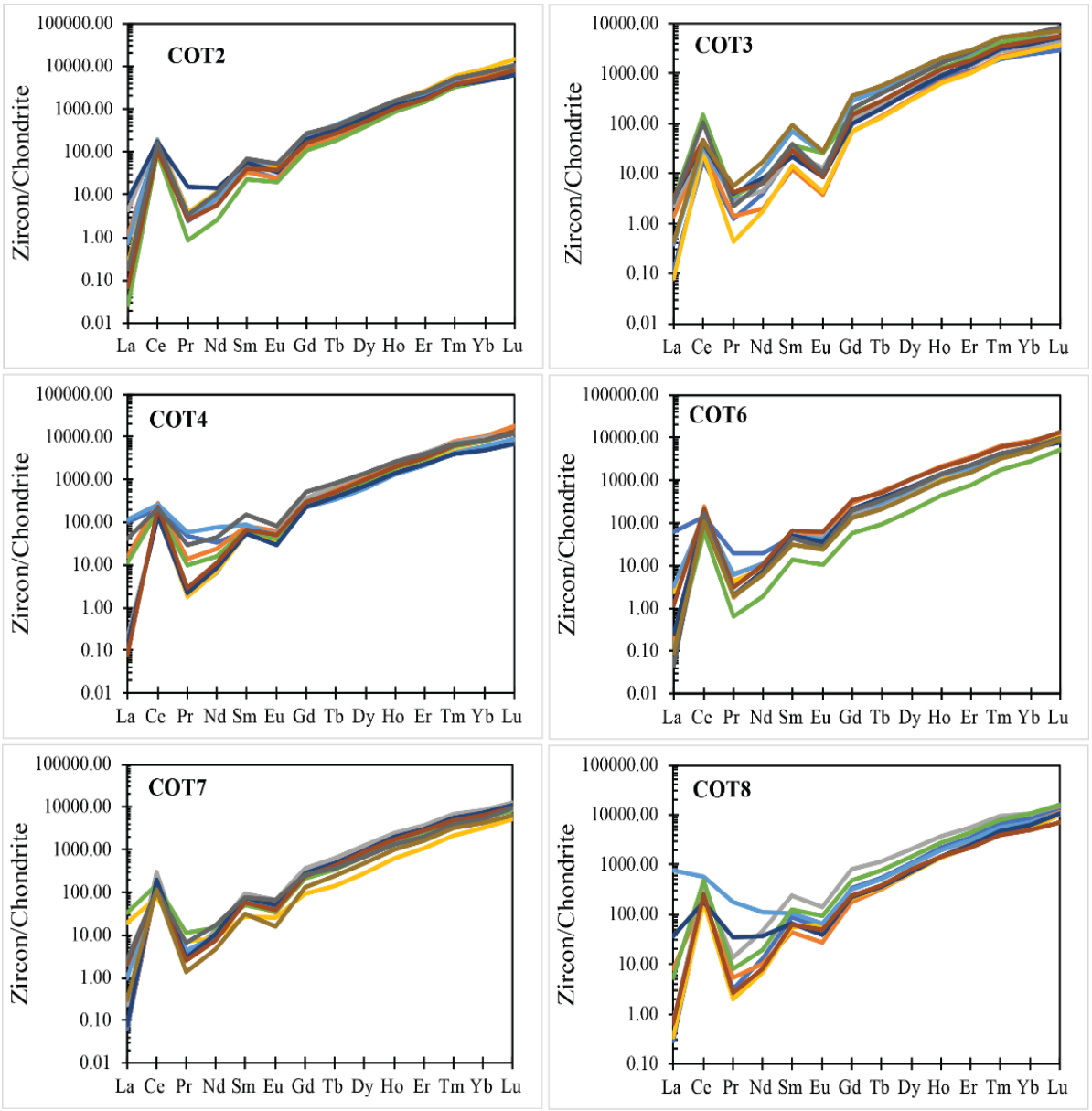

Figure 5. Chondrite-normalized rare-earth element (REE) patterns for zircon in samples for transect 1.

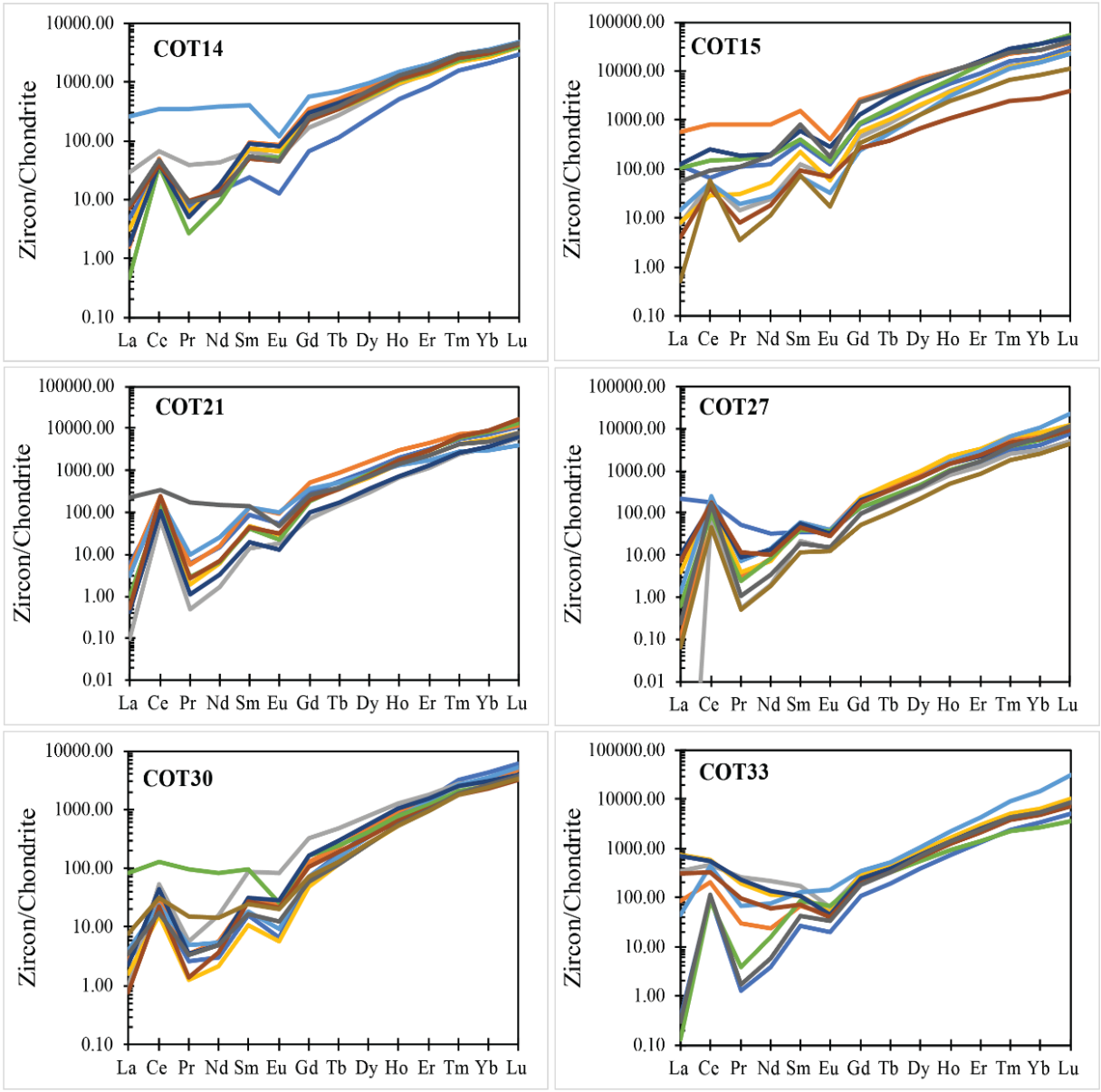

Figure 5 cont. Chondrite-normalized rare-earth element (REE) patterns for zircon in samples for transect 2.

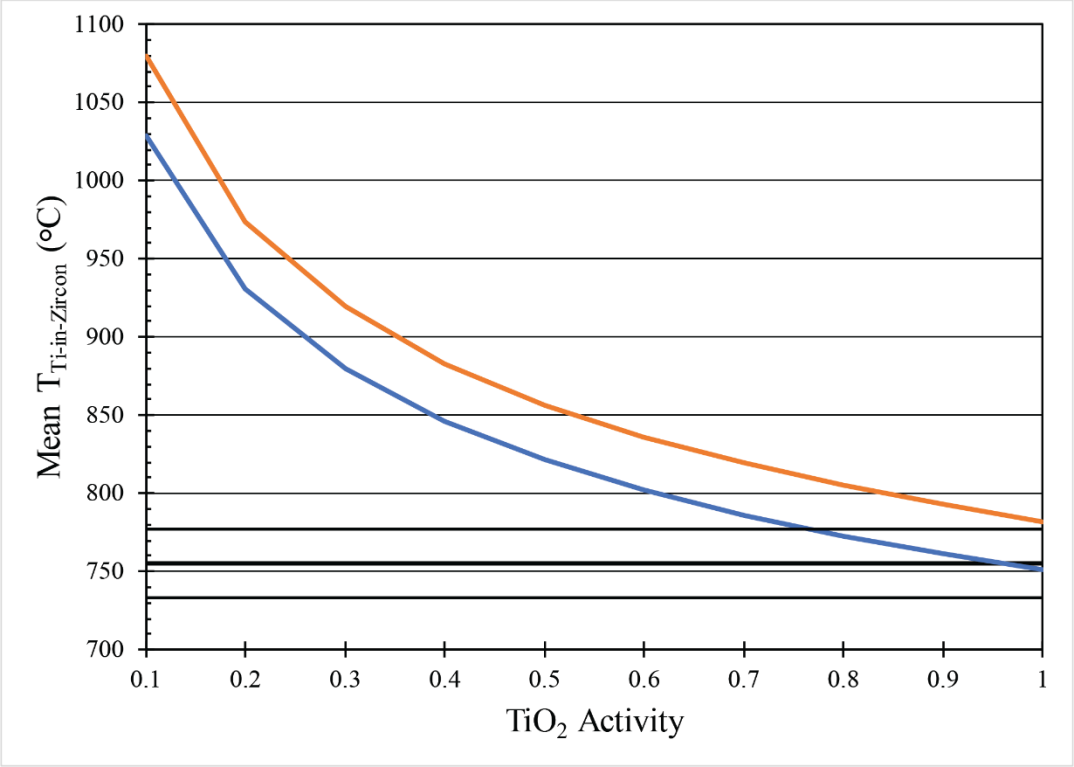

Figure 6. Average Titanium-in-zircon temperatures (°C) versus Ti activity (α_{TiO2}) activity. Proper and accurate application of the thermometer requires knowledge of α_{TiO2} and α_{SiO2} at the time of zircon crystallization. A range of α_{TiO2} were evaluated to ensure correct activities were selected. The activity of SiO_2 was set to 1. Black line represents Al-in-Hornblende crystallization temperatures of the batholith. Dashed lines are the calculated maximum and minimum Al-in-zircon temperatures.

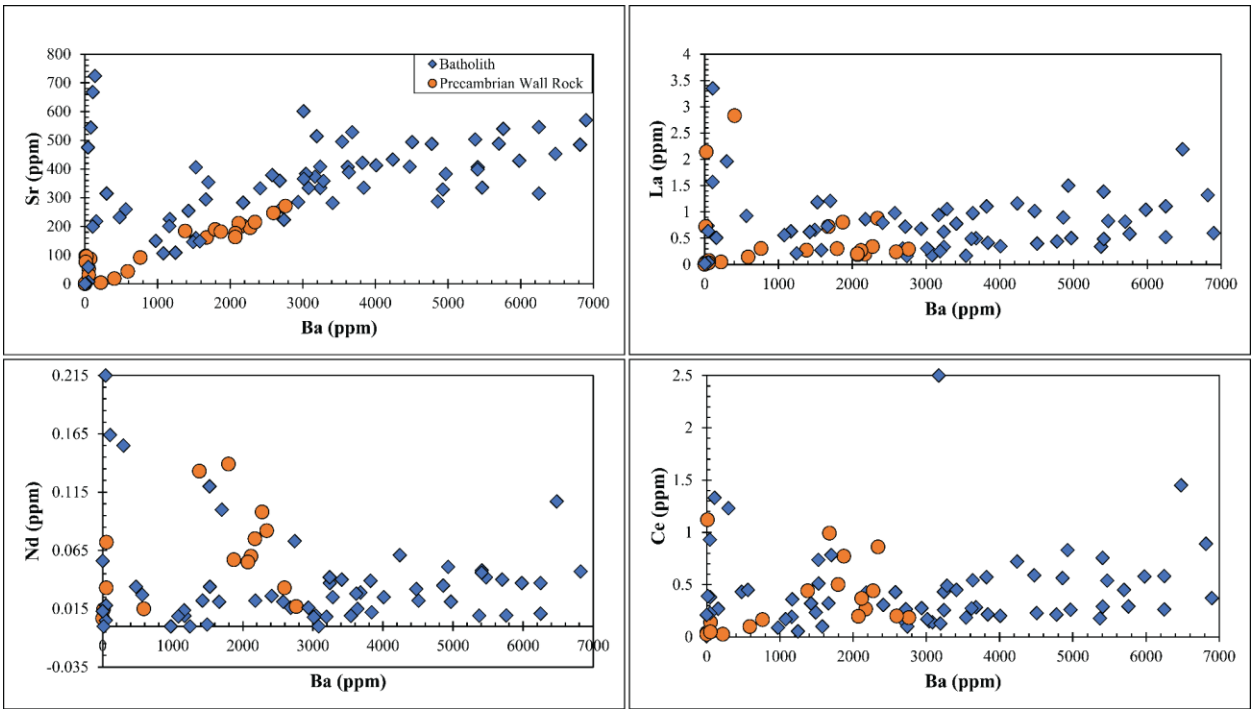

Figure 7. Bivariate trace element plots for *in situ* spots in K-feldspar: La versus Ba, Sr versus Ba, Ce versus Ba, and Nd versus Ba.

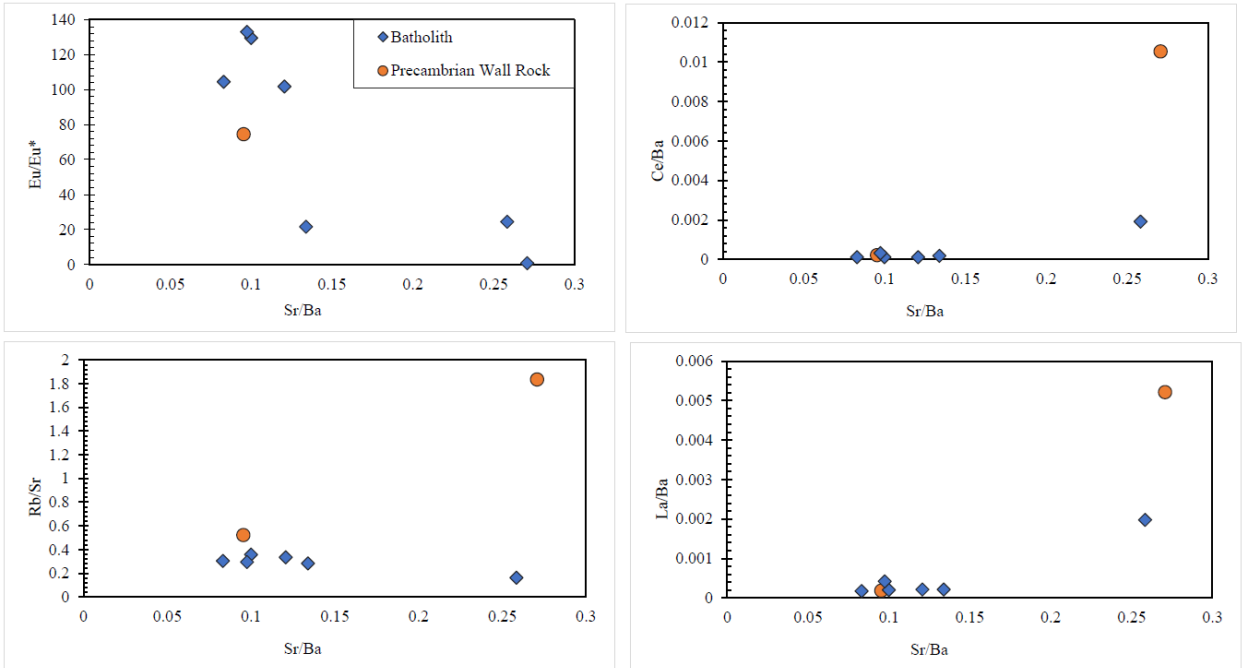

Figure 8. Ratio bivariate trace element plots for average K-feldspar: Eu/Eu* versus Sr/Ba, Ce/Ba versus Sr/Ba, Pb/Sr versus Sr/Ba, and La/Ba versus Sr/Ba.

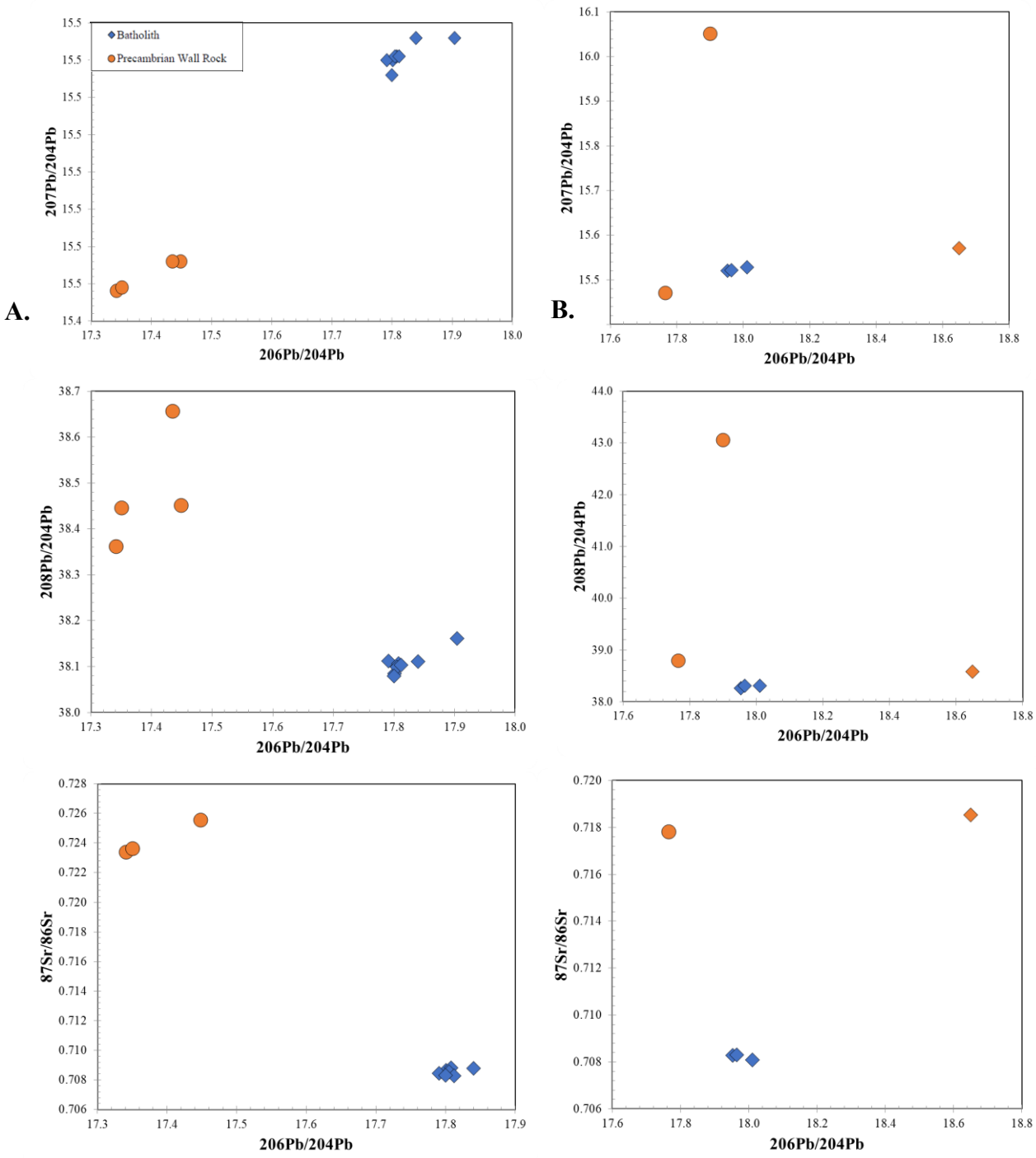

Figure 9a. Mineral radiogenic isotope plots of K-feldspar: $^{207}Pb/^{204}Pb$ versus $^{206}Pb/^{204}Pb$, $^{208}Pb/^{204}Pb$ versus $^{206}Pb/^{204}Pb$, and $^{87}Sr/^{86}Sr$ versus $^{206}Pb/^{204}Pb$.

Figure 9b. Whole rock radiogenic isotope plots: $^{207}Pb/^{204}Pb$ versus $^{206}Pb/^{204}Pb$, $^{208}Pb/^{204}Pb$ versus $^{206}Pb/^{204}Pb$, and $^{87}Sr/^{86}Sr$ versus $^{206}Pb/^{204}Pb$.

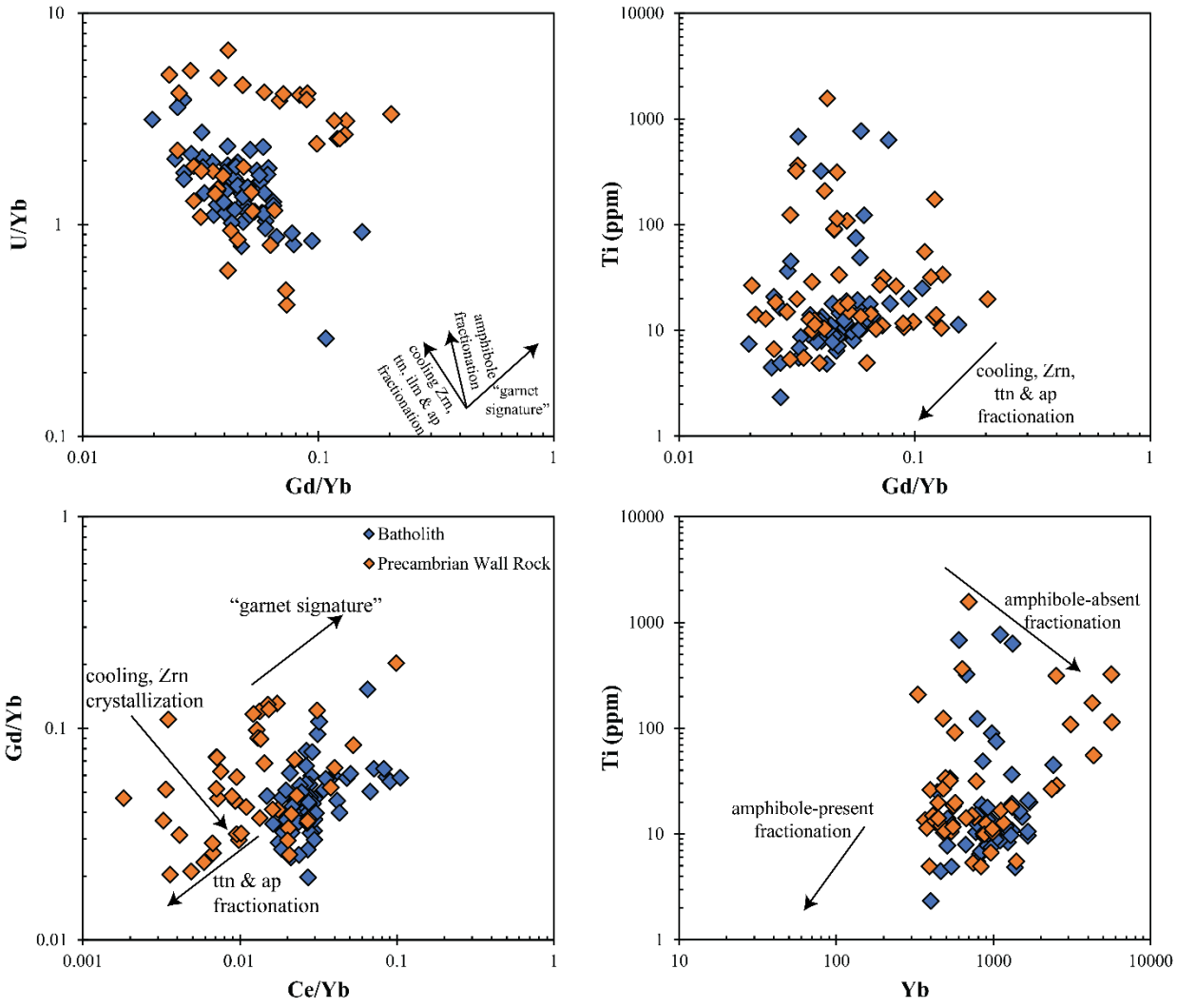

Figure 10. Zircon trace element ratios recording process during magma cooling. These ratios demonstrate conditions during fractionation and cooling: U/Yb versus Gd/Yb, Ti versus Gd/Yb, Gd/Yb versus Ce/Yb, and Ti versus Yb.

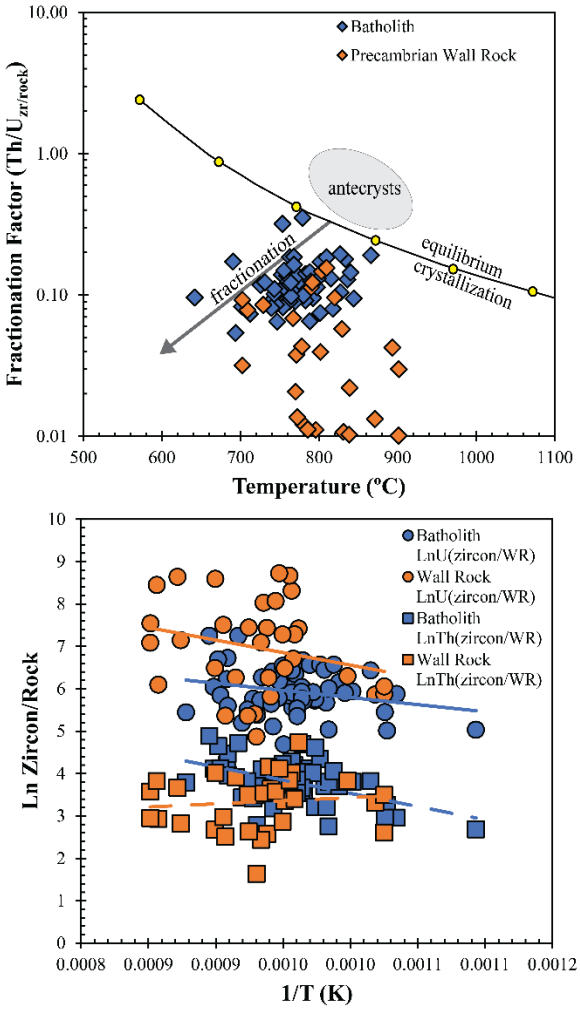

Figure 11. Zircon process record vs temperature demonstration conditions during fractionation and equilibrium of the Mt. Princeton Batholith: Fractionation factor versus temperature and Ln Zircon/Rock versus 1/T (K). Fractionation factors are below the calculated equilibrium crystallization temperature of magma and Th and U contents suggest zircons are dominantly crystallized in the magma and not inherited from the source or wall rock.

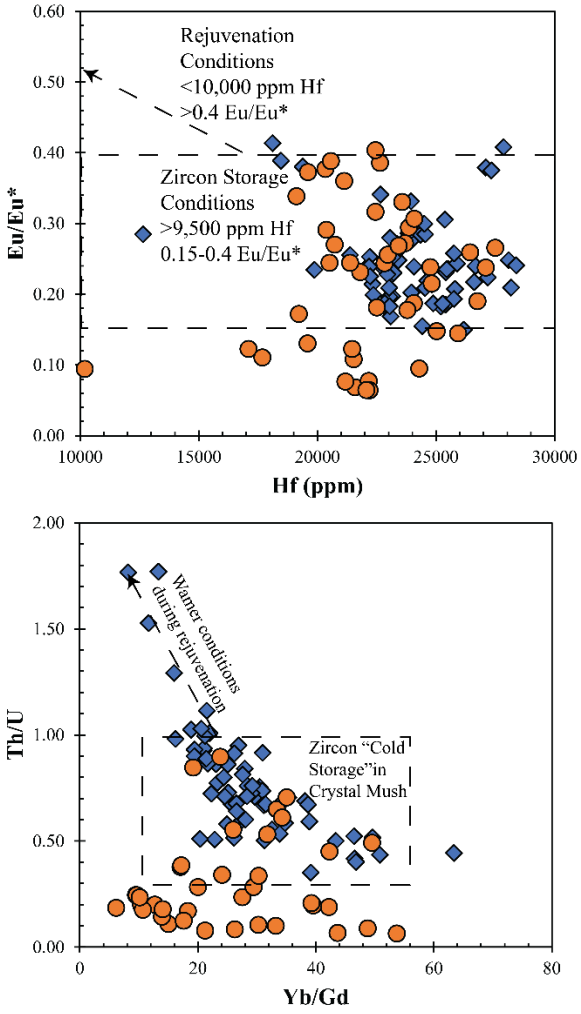

Figure 12. Concentration at zircon storage conditions: Eu/Eu* versus Hf and Th/U versus Yb/Gd. Zircon Th/U and Yb/Gd ratios, Eu/Eu* and Hf contents suggest zircon crystallized and was stored in "cold storage" conditions during emplacement. Some Precambrian wall rock zircons show signatures of reheating likely the result of emplacement and small percent assimilation by the Mt. Princeton monzogranite magma. Storage and reheating fields suggested by Klemetti and Clynne (2014).

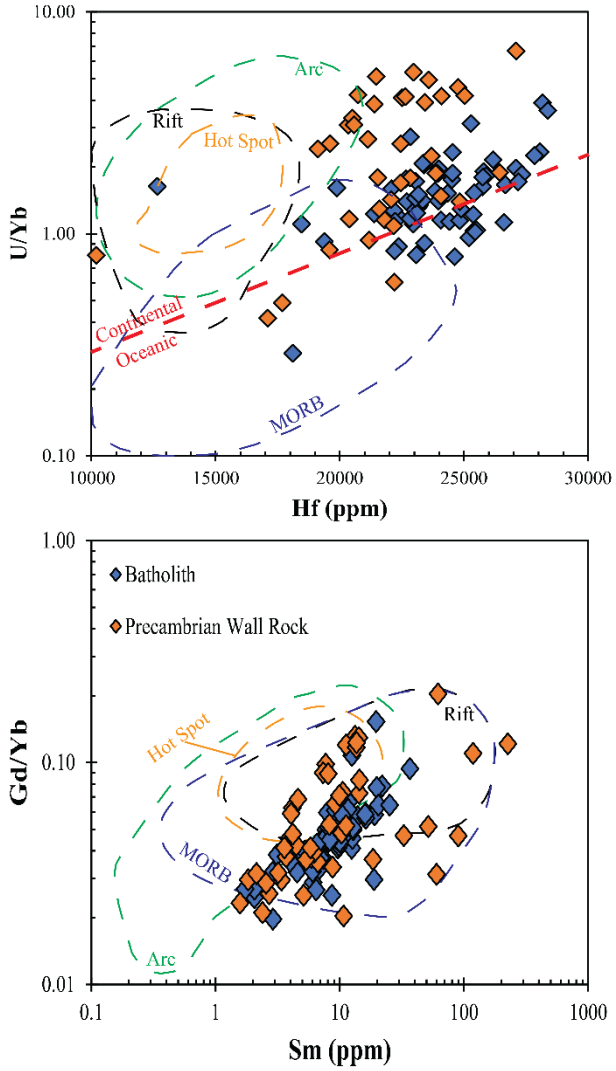

Figure 13. Formation of zircon across tectonic environments: U/Yb versus Hf and Gd/Yb versus Sm.

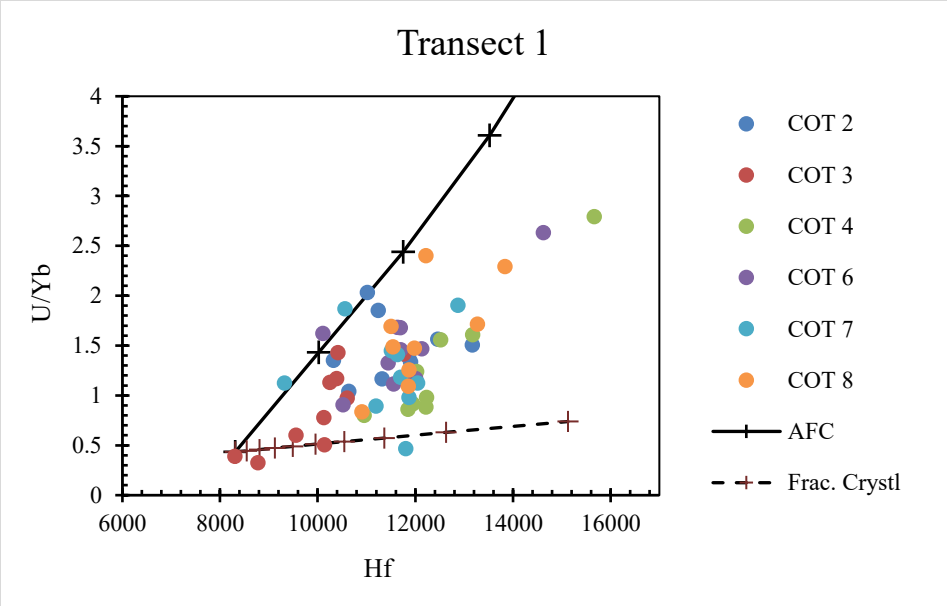

Figure 14. Assimilation and fractional crystallization patterns for transect 1 based on zircon trace element contents. Symbols along the AFC and fractionation trends are in 1% increments. Trends suggest assimilated magmas mixed with fractionated granitic magmas with decreasing impact of the wall rock away from the magma-wall rock interface.

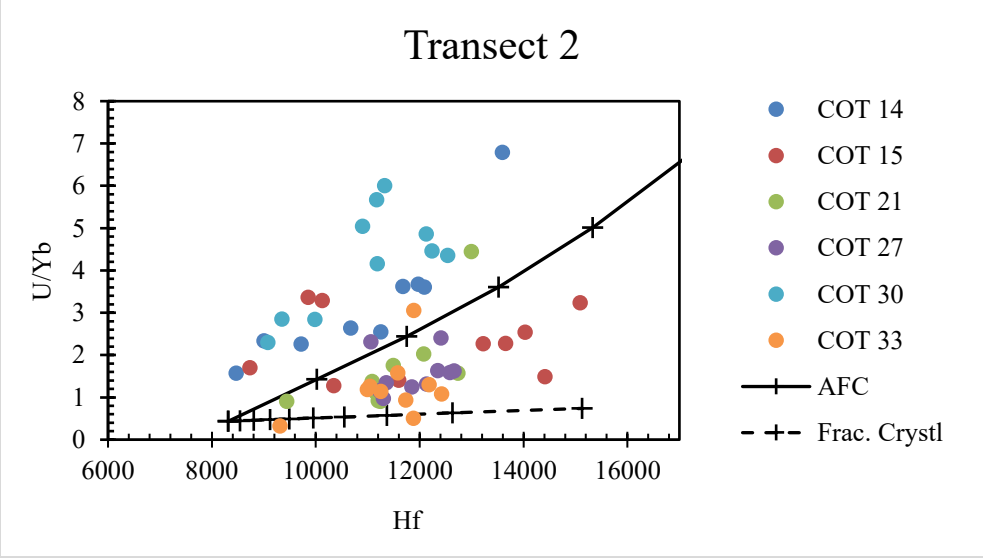

Figure 15. Assimilation and fractional crystallization patterns for transect 2. Symbols along the AFC and fractionation trends are in 1% increments. Trends suggest assimilated magmas mixed with fractionated granitic magmas with decreasing impact of the wall rock away from the magma-wall rock interface. Precambrian age zircons and inherited zircons fall off the AFC trend and do not fit the model.

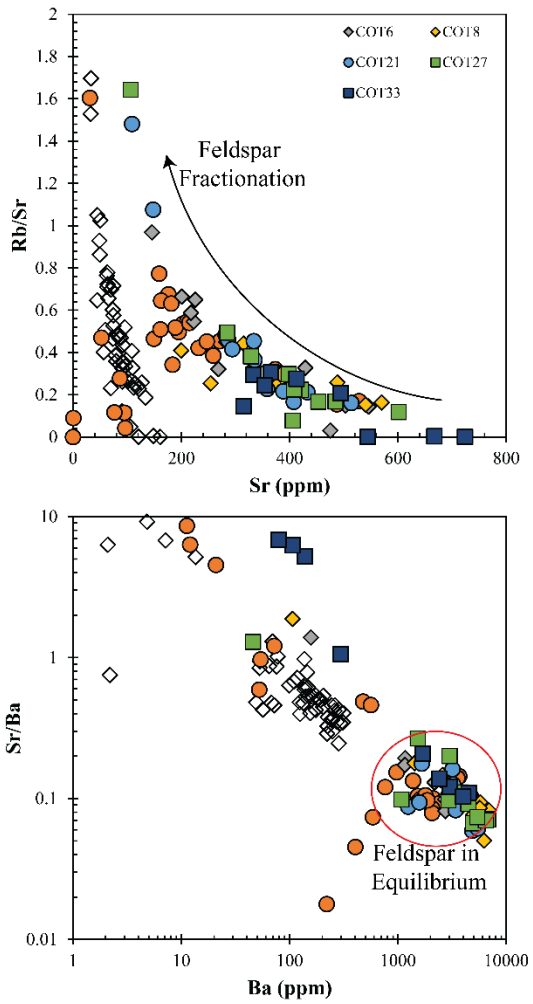

Figure 16. Feldspar trace element ratios versus Sr and Ba contents. Open diamonds represent magma composition in equilibrium with the K-feldspars at the time of crystallization. Partition coeffiencts of Ba, Sr and Rb are 22, 2.5 and 2.85, respectively. Clusters of data points suggest equilibrium of K-feldspar with the magma. showing concentrations at equilibrium and during fractionation of K-feldspar: Rb/Sr versus Sr and Sr versus Ba.

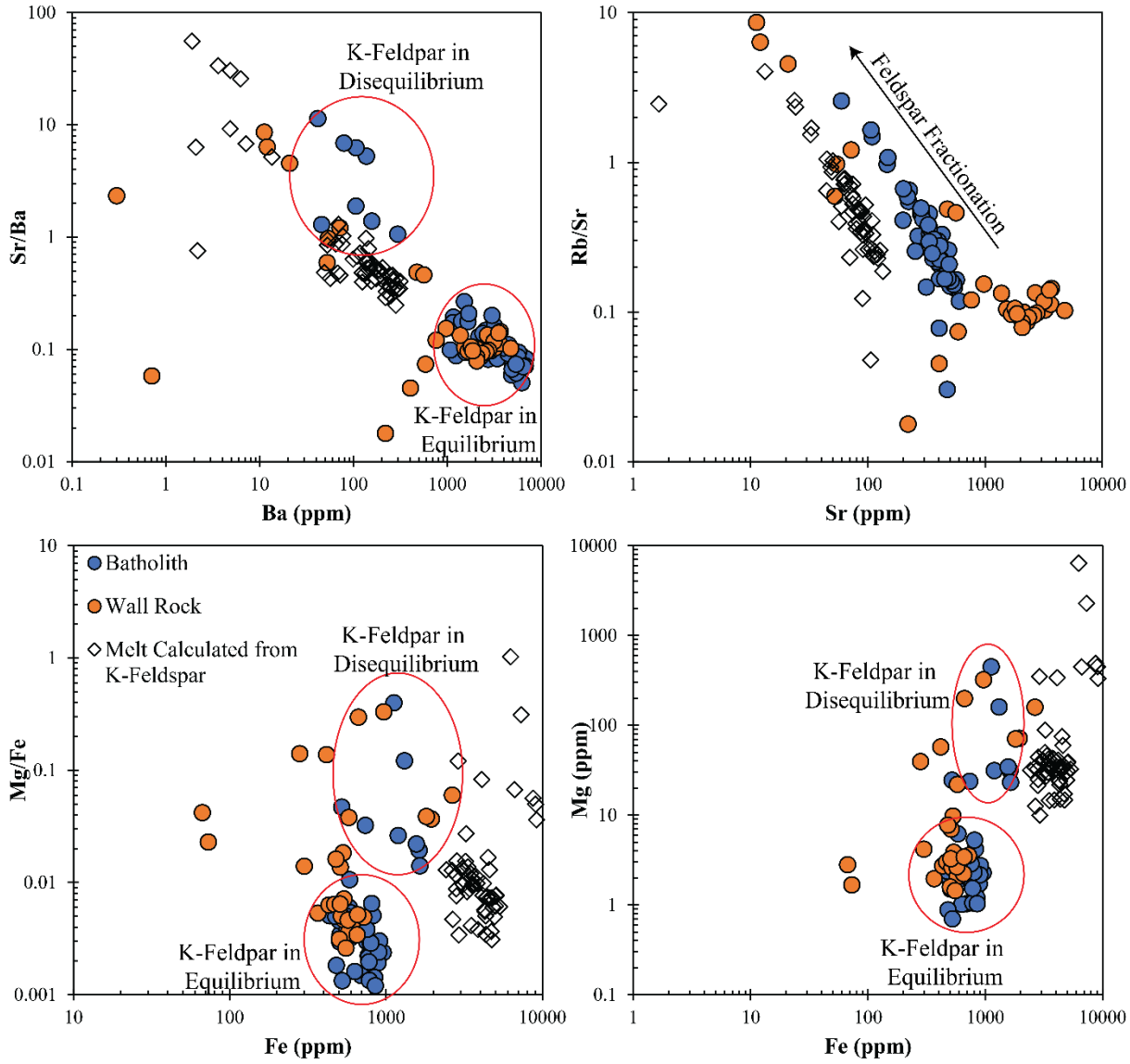

Figure 17. Equilibrium determination in K-feldspar showing concentrations at disequilibrium, equilibrium, and during fractionation of K-feldspar: Sr/Ba versus Ba, Rb/Sr versus Sr, Mg/Fe versus Fe, and Mg versus Fe.

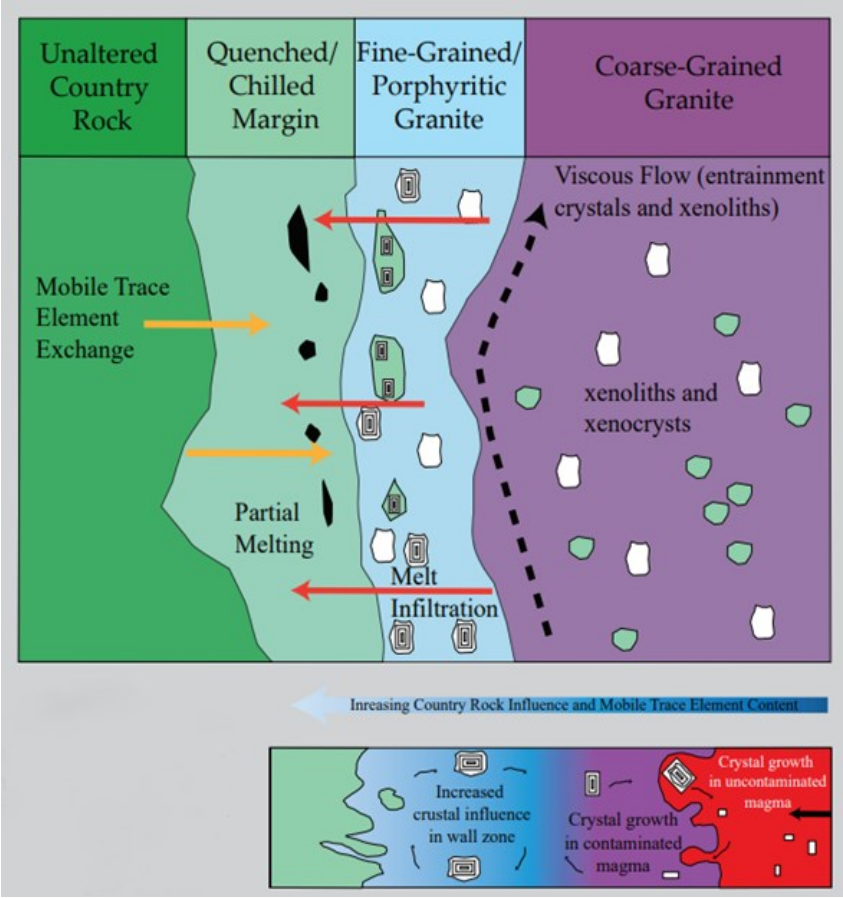

Figure 18. Cartoon illustration showing specifically, granitic composition magmatic bodies and their partial dissolution and incorporation of the wall rock interface at a chilled margin (similar to Michelfelder and LaRue, 2020).

APPENDICES

Appendix 1: Petrographic Image Stills

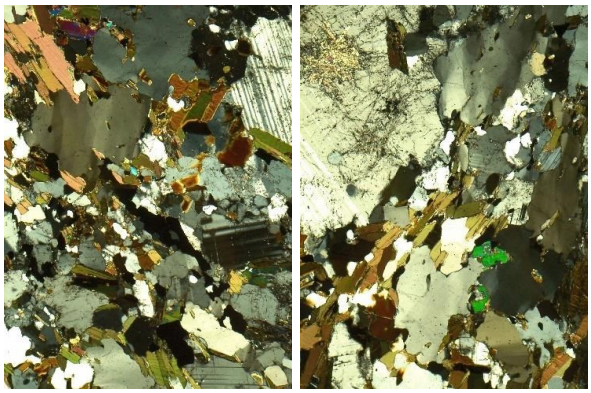

COT 1 – 10x magnification XPL: varietal (biotite) and accessory (Mg-Ti oxides) minerals follow notable foliation orientations. Alteration of plagioclase to sericite is significant in the center of mineral grains.

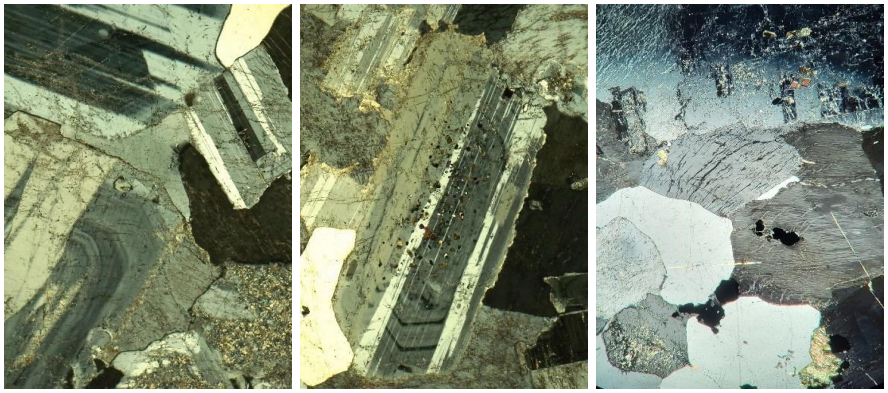

COT 2 – 10x magnification XPL: these stills demonstrate concentric zoning of calcic plagioclase grains as well as evidence of inheritance. Myrmekite and Perthite shown in the third image.

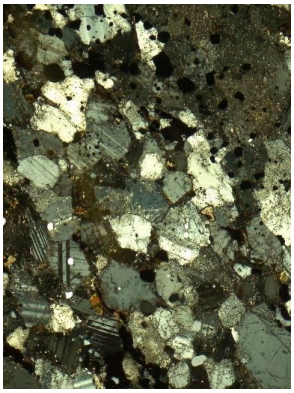

COT 3 – 10x magnification XPL: pervasive alteration products follow foliation, grain sizes average at or less than 1.2mm.

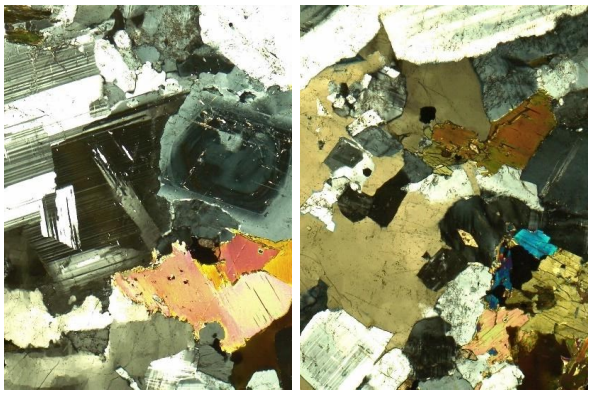

COT 4 – 10x magnification XPL: concentric zoning in some plagioclase grains surrounded by others that are more calcic in composition (indicated by polysynthetic and albitic twinning). Undulatory extinction in quartz grains. Alteration includes Ti-rich biotite to chlorite and feldspar to sericite. Titanite and apatite also present in these stills.

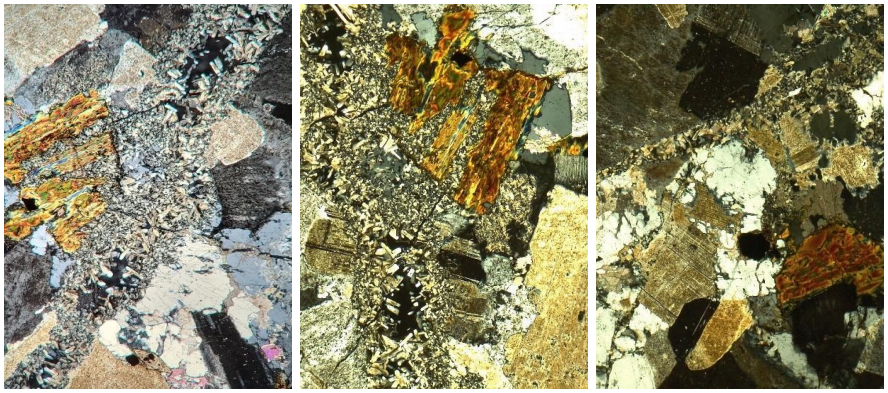

COT 7 – 10x magnification XPL: Located very near a fault and thus heavily altered throughout. Cumulate fracture fill of primarily quartz is also present.

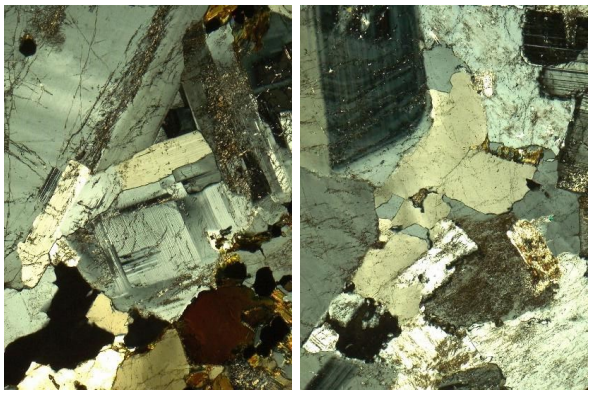

COT 8 – 10x magnification XPL: Plagioclase altering to sericite with included apatite.

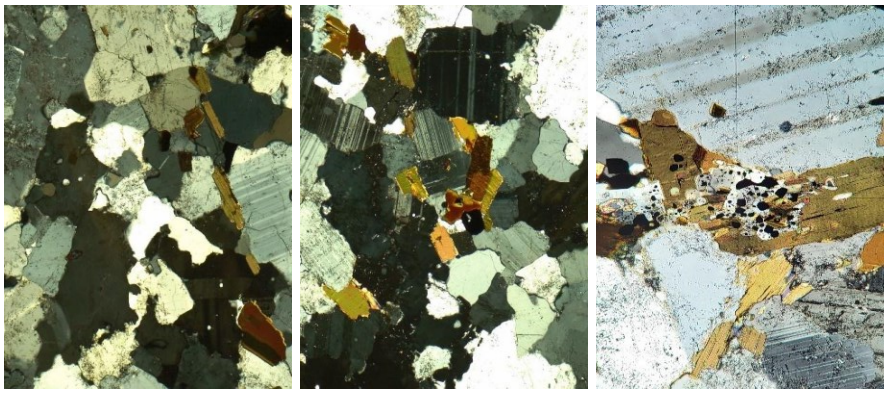

COT 14 – Sizable biotite forming in clusters in and around glomerocrysts of amphibolite. Alteration of biotite to chlorite and amphibole to epidote.

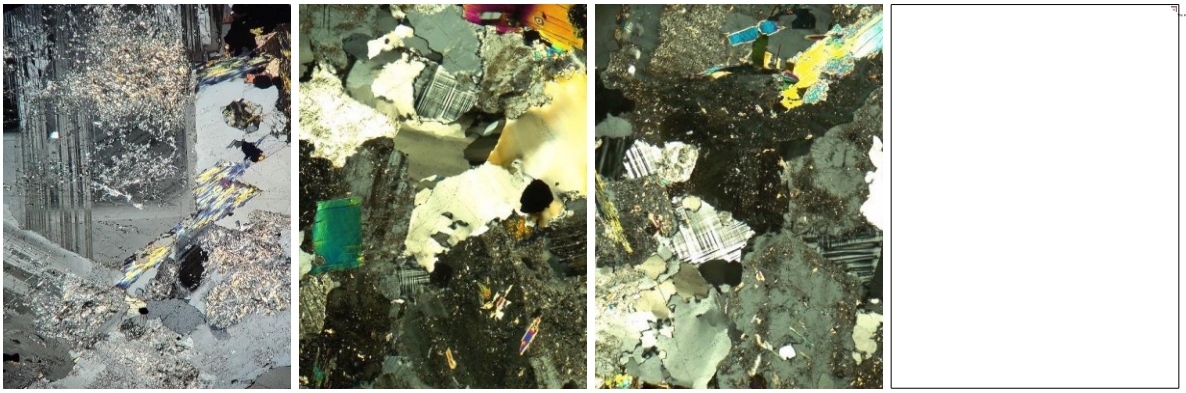

COT 15 – 10x magnification XPL of pervasive alteration products in the Precambrian host rock at the magma-wall rock interface. Zoisite present as alteration products alongside sericite and chlorite.

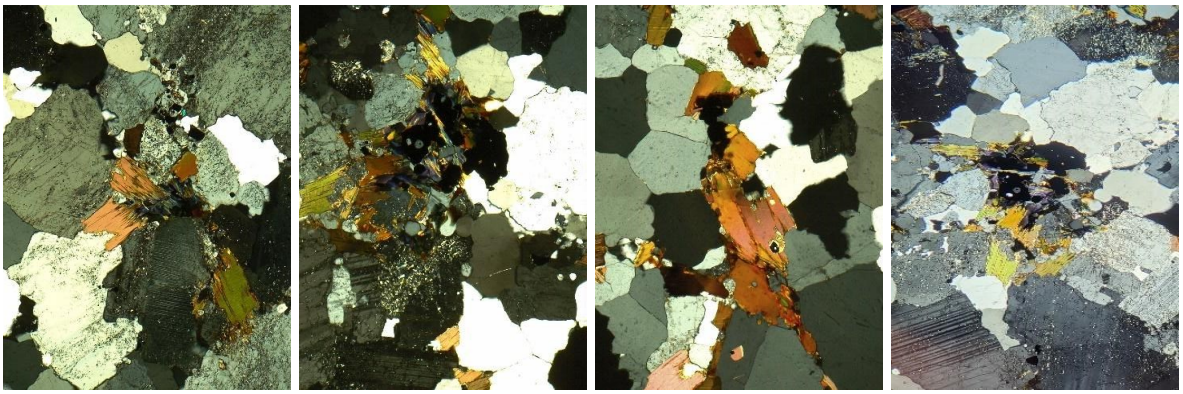

COT 18 – 10x magnification XPL: an even modal across essential minerals informing on a monzonite. Biotite, amphibole and oxides in glomerocrysts.

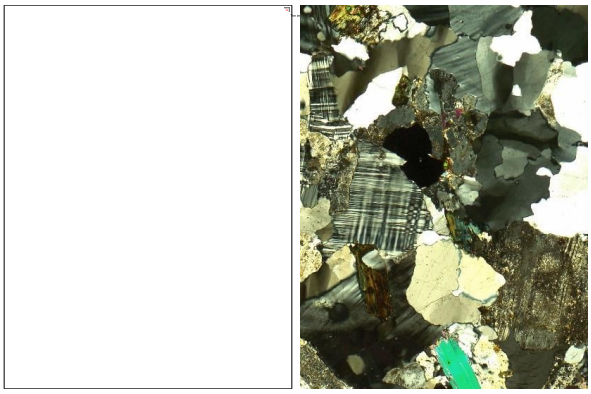

COT 20 – 10x magnification XPL: Clinozoisite percentages increase from previous samples as varietal minerals decrease in size.

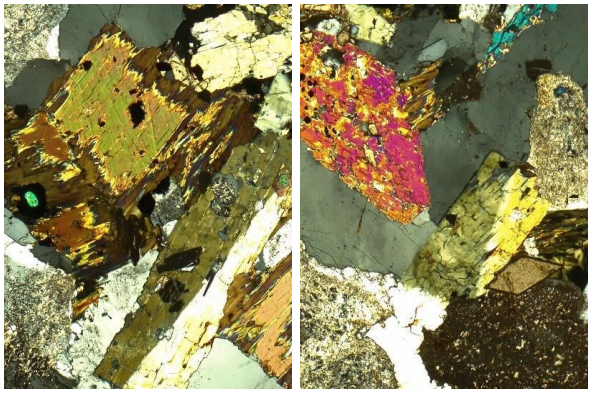

COT 21 – 10x magnification XPL: oxides cluster around amphibolites.

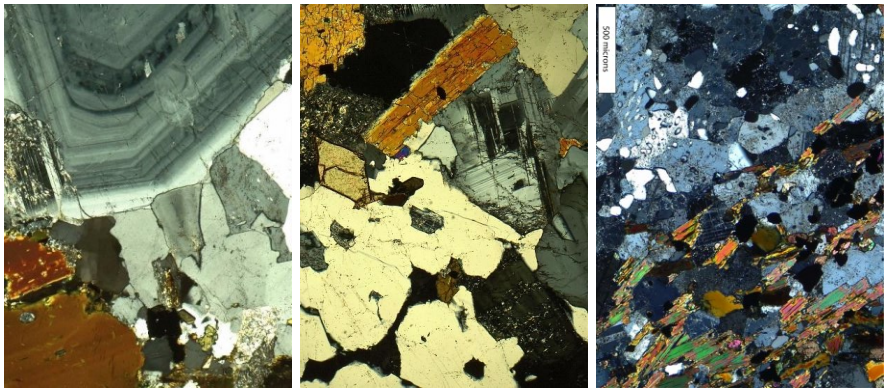

COT 27 - 10x magnification XPL of Precambrian lens contact to the interior quartz monzonite. Amphibolitess and oxides increase in size and abundance. Plagioclase and quartz also increase in size and abundance.

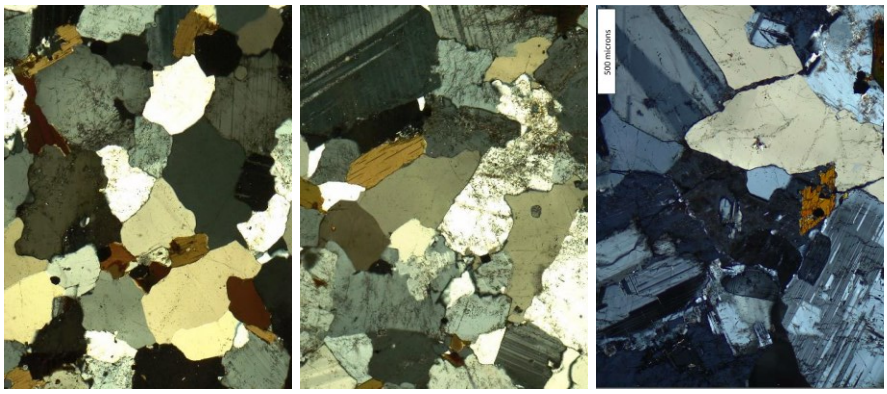

COT 30 - 10x magnification XPL of a “clean” example of the interior monzogranite.

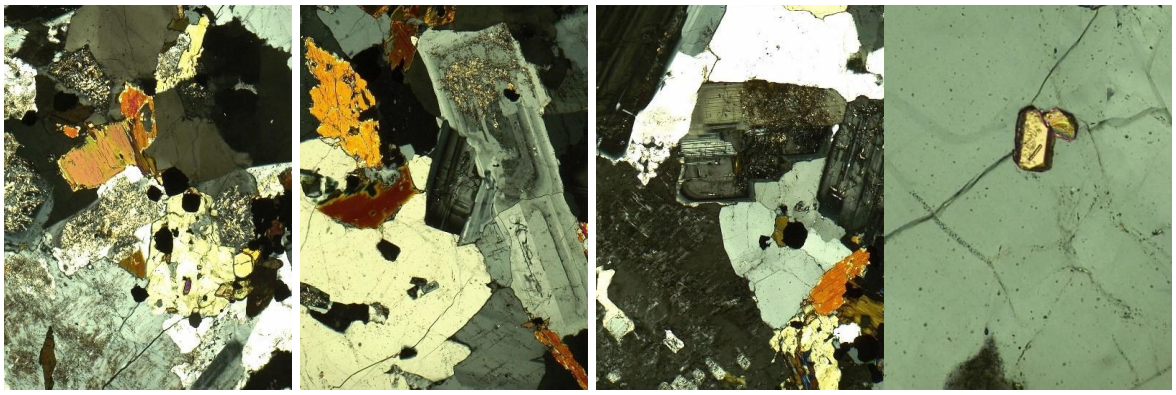

COT 33 – 10x magnification XPL: zoned zircon grains and zircon trapped as melt inclusions within apatite are present. Less alteration is present in biotite and essential minerals increase in size.

Appendix 2: BSE Images

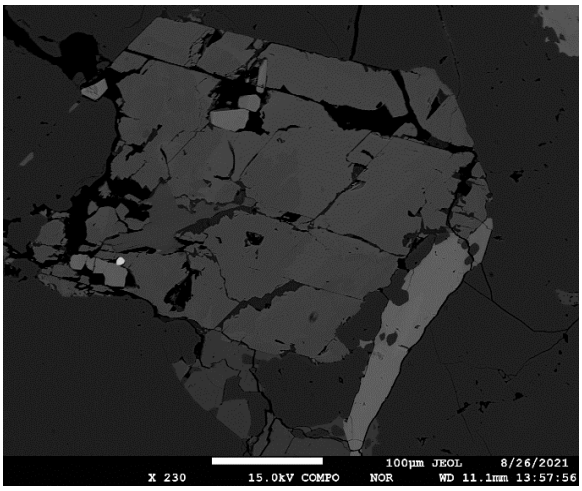

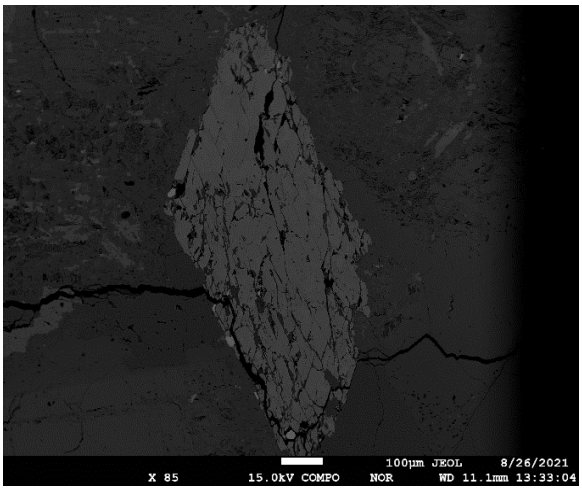

COT 21 K-feldspar

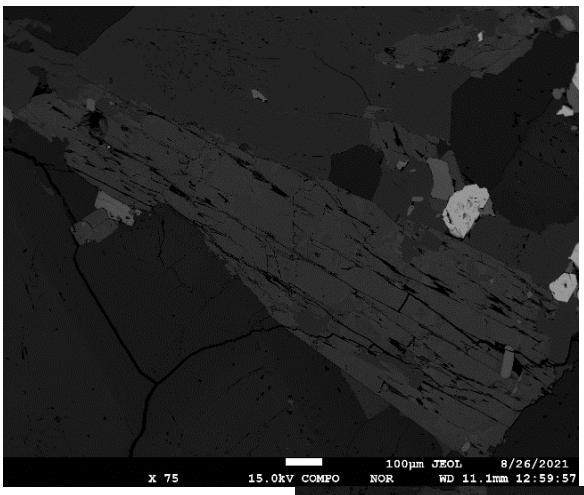

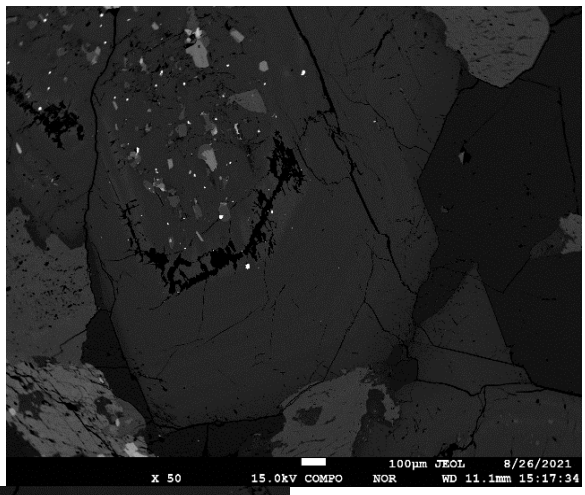

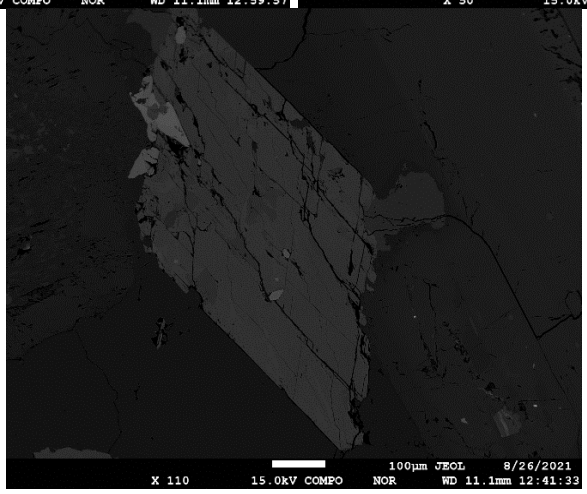

COT 27 K-feldspar

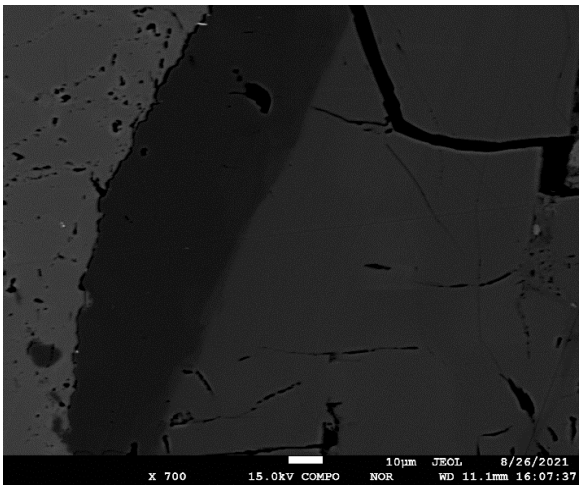

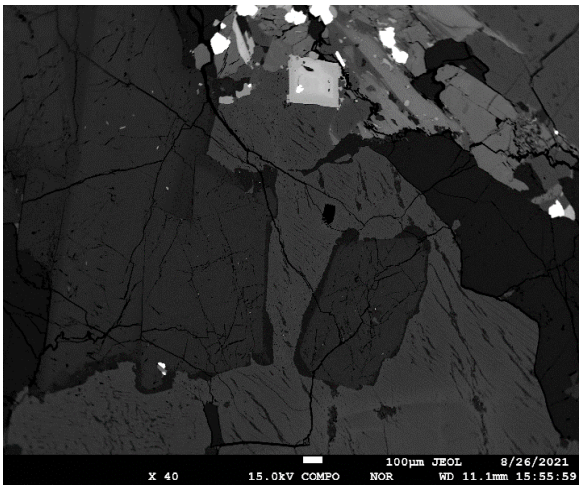

COT 33 K-feldspar

Appendix 3: U-Pb Age Pick and Concordia

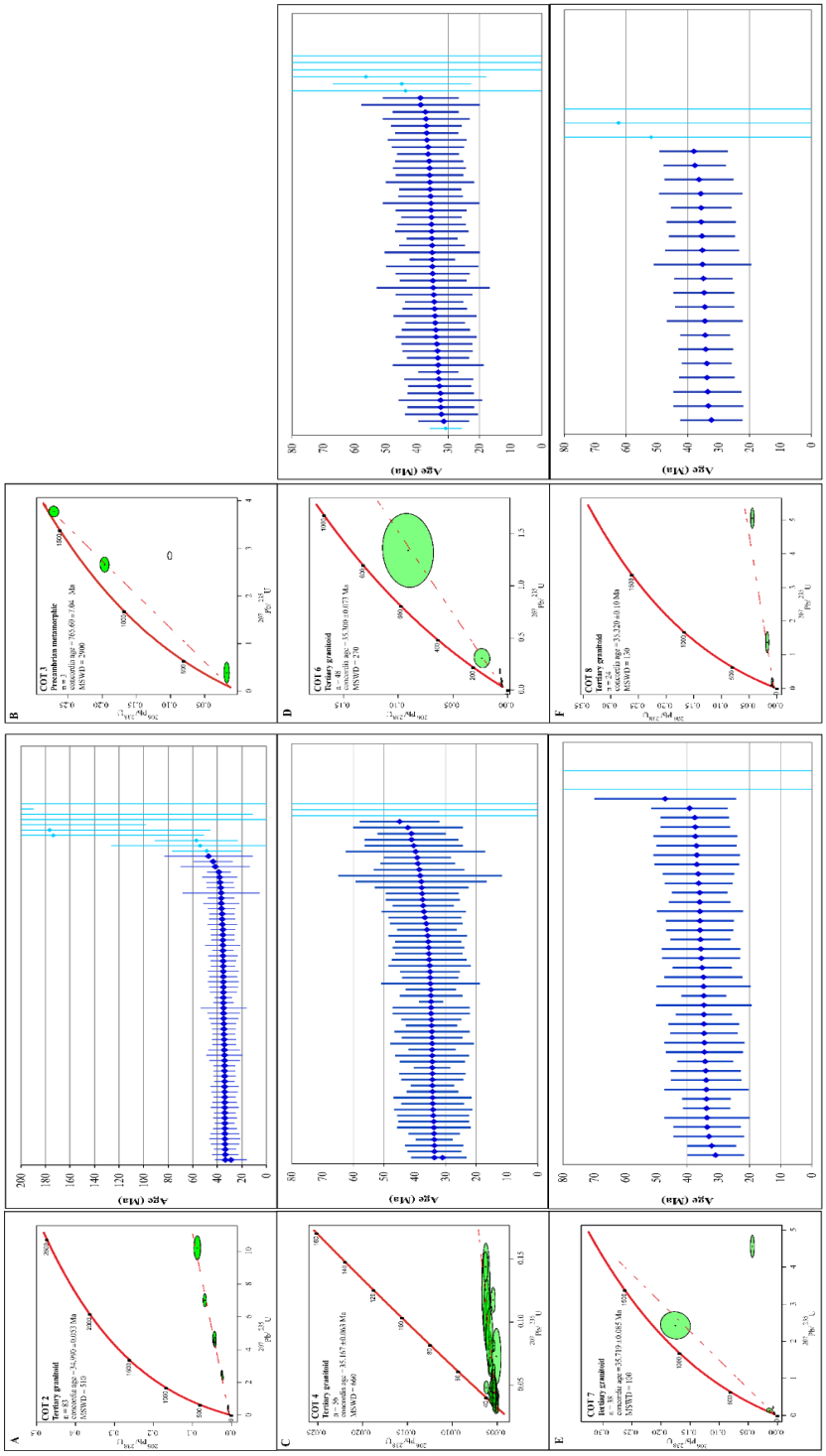

Zircon U-Pb weighted mean plots and Wetherill Concordia diagrams for samples from transect 1. Zircon ages highlighted in light blue in the weighted mean plots were discarded from age calculations based on criteria discussed in text. Sample COT3 only contained three zircon analyses and a weighted mean plot was not statistically significant.

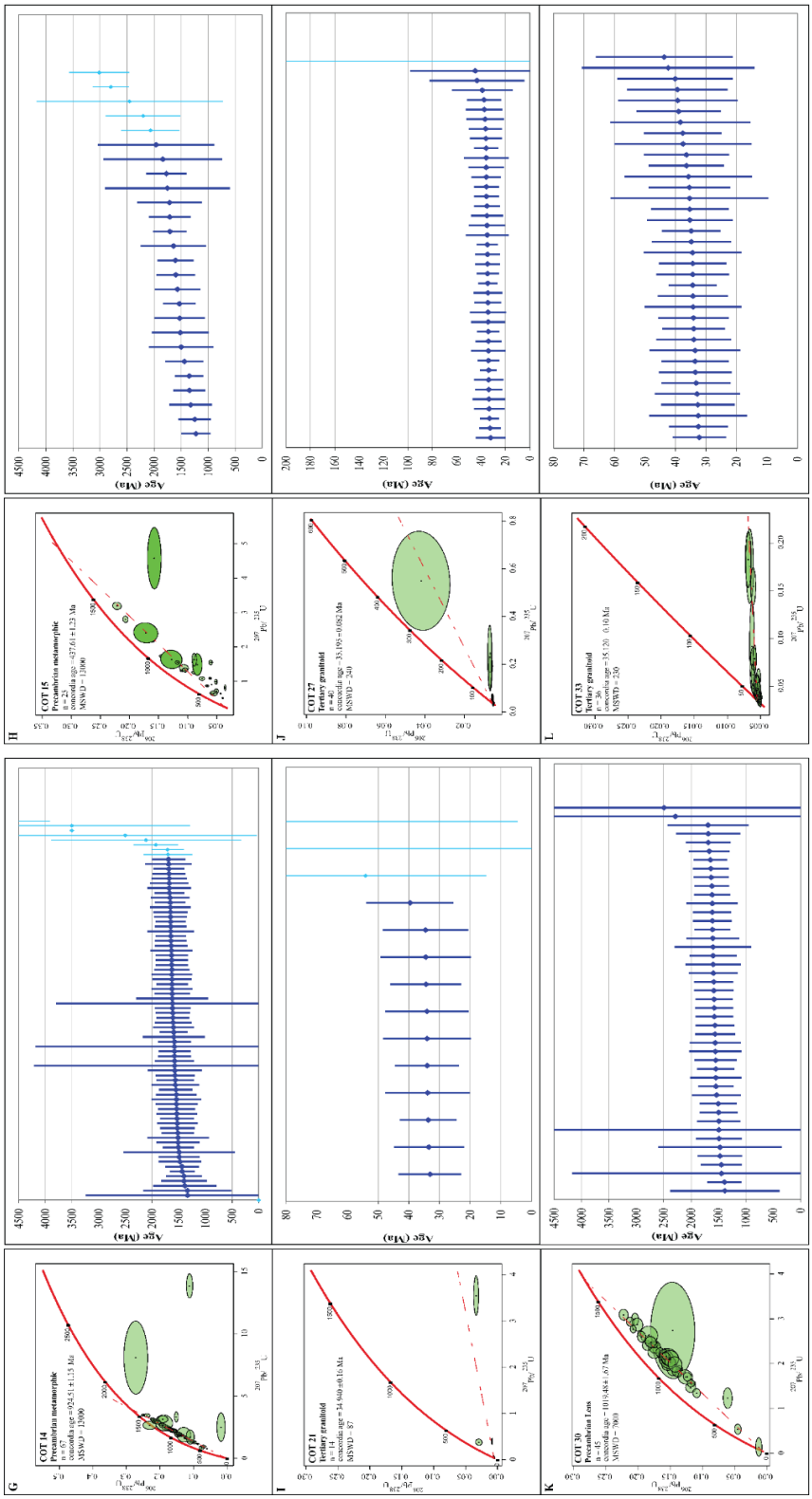

Zircon U-Pb weighted mean plots and Wetherill Concordia diagrams for samples from transect 2. Zircon ages highlighted in light blue in the weighted mean plots were discarded from age calculations based on criteria discussed in text.

Appendix 4: Zircon U-Pb Geochronology Full Dataset

Appendix 5: Zircon Trace Element Full Dataset

Appendix 6: Mineral (K-feldspar) Trace Element and Radiogenic Isotope Full Dataset

Appendix 7: Hornblende Major Element Full Dataset

Appendix 8: Whole Rock Trace Element and Radiogenic Isotope Full Dataset

Appendices 4-8 see following doi link for complete datasets

Michelfelder, Gary; Bohannon, Loren (2022), "Bohannon, Loren Thesis Supplementary Data Nov. 2022", Mendeley Data, V1, doi: 10.17632/hcfnfmb9hy.1.

https://data.mendeley.com/datasets/hcfnfmb9hy/1